
DISENTANGLING VISUAL EMBEDDINGS WITH MINIMAL DISTRIBUTIONAL ASSUMPTIONS

Tobias Leemann*

University of Tübingen

tobias.leemann@uni-tuebingen.de

Michael Kirchhof*

University of Tübingen

michael.kirchhof@uni-tuebingen.de

Yao Rong

University of Tübingen

yao.rong@uni-tuebingen.de

Enkelejda Kasneci

Technical University of Munich

enkelejda.kasneci@tum.de

Gjergji Kasneci

University of Tübingen

gjergji.kasneci@uni-tuebingen.de

ABSTRACT

Interest in understanding and factorizing embedding spaces learned by deep encoders is growing. Concept discovery methods search the embedding spaces for interpretable latent components like *object shape* or *color* and disentangle them into individual axes in the embedding space. Yet, the applicability of modern disentanglement learning techniques or independent component analysis (ICA) is limited when it comes to vision tasks: They either require training a model of the complex image-generating process or their rigid stochastic independence assumptions on the component distribution are violated in practice. In this work, we identify components in encoder embedding spaces without distributional assumptions and without training a generator. Instead, we utilize functional compositionality properties of image-generating processes. We derive two novel post-hoc component discovery methods and prove theoretical identifiability guarantees. We study them in realistic visual disentanglement tasks with correlated components and violated functional assumptions. Our approaches stably maintain superior performance against 300+ state-of-the-art disentanglement and component analysis models.

1 INTRODUCTION

Modern computer vision systems represent images in high-dimensional embedding spaces. To unveil why an image is considered to be similar to a certain class, interest in understanding these embeddings, e.g., via conceptual explanations [24, 27, 12, 48, 1, 22], is increasing. The goal is to scrutinize a given encoder by decomposing its embedding space into interpretable directions post-hoc, i.e., after training. In the optimal case, each direction corresponds to exactly one interpretable concept of an image at a time. Yet, the problem of concept discovery, i.e., finding such interpretable directions, is hard and its definition is still a topic of discussion [29, 48].

Concurrently, disentanglement learning [17, 8, 30] offers a more formal perspective on the problem. Here, it is also assumed that there exist interpretable ground-truth components. Images are seen as random samples from the distribution of these components, which are decoded into the image-domain via an image-generating process. The goal is to build a generative model with an embedding-space that is *disentangled*, i.e., each latent dimension corresponds to precisely one ground-truth component. There is a growing body of literature on the conditions under which this can be theoretically guaranteed [21, 18, 49], which are known as *identifiability* conditions. This begs the question: *Can these identifiability guarantees be transferred to the (visual) concept discovery setting?*

There are two fundamental differences that make the task challenging. First, disentanglement learning usually trains generators, while in post-hoc concept discovery we receive an encoder only, already trained, e.g., on a visual classification task. Second, the conditions required by many identifiability conditions in disentanglement learning are not fulfilled in practical vision scenarios. One of these is the assumption of stochastic independence of the ground-truth

*Equal contribution

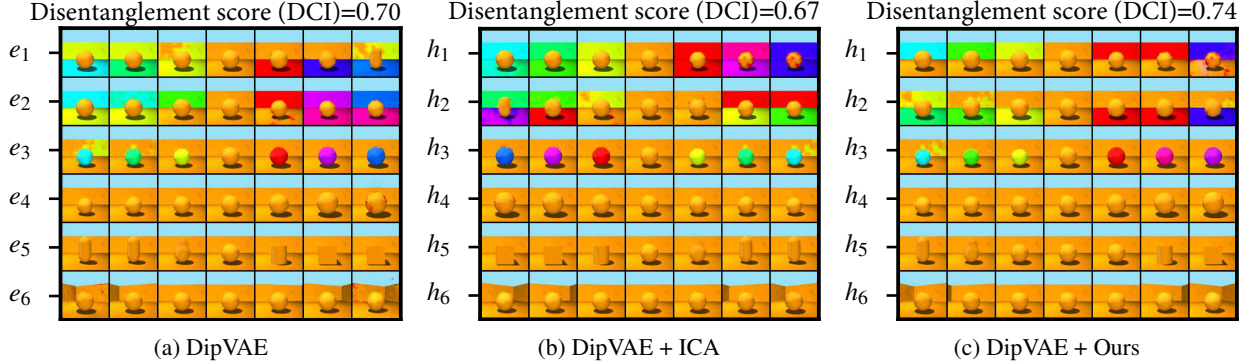


Figure 1: (a) Traversals along each embedding space axis e_k of the best disentanglement model (DipVAE). The components *floor color* and *background color* were correlated in the training data. DipVAE struggles to disentangle them into e_1 and e_2 individually. (b) Because of the correlation and the isotropic structure of the embedding space, ICA also fails to find these directions h_k post-hoc. (c) Our disjoint attributions approach is able to separate the correlated components into h_1 and h_2 .

components [20, 19, 18]. Recently, Träuble et al. [43] have shown that even if just two components of a dataset are correlated, current disentanglement learning methods fail. Fig. 1a shows an example: If we move along the unit directions e_1, e_2 in the embedding space of this state-of-the-art disentangling model, the (correlated) components *floor color* and *background color* should change independently. This is not fulfilled, and likewise the directions h_k that ICA discovers post-hoc are not disentangled either (Fig. 1b).

In this paper, we seek a powerful concept discovery approach that is (1) applicable to embedding spaces of trained visual encoders post-hoc, (2) has a theoretical identifiability guarantee, thus mapping each discovered concept direction to precisely one meaningful ground-truth component, but (3) does not require distributional assumptions.

To date, there is no such method. Yet, the works on disentanglement learning constitute a promising starting point. Their core idea is to re-model the process that generated the data. While most works approach this in terms of distributional properties, we think about how the images were generated from the ground-truth concepts from a *functional* perspective. In particular, we propose utilizing *visual compositionality properties*, i.e., that components usually affect either disjoint or at least orthogonal regions of an image. We prove a *transfer lemma*, which shows that these properties of the image-generating process also leave a “trace” in the encoders learned from a set of data samples. This finding permits to construct two novel post-hoc concept discovery methods that search for each of these traces in encoders’ embedding spaces. We prove identifiability guarantees for discovering disentangled components, even if they are correlated. We confirm this experimentally under various visual encoder setups and also test the robustness of these functional approaches to violations of their assumptions.

In summary, our work offers the following contributions: (1) We propose a *transfer lemma* that transfers functional traces of the data-generating process to encoder embedding spaces. (2) We derive the *disjoint attributions (DA)* and the less constrained *orthogonal attributions (OA)* criterion. We prove that they identify the disentangled original components up to permutation and scale. (3) We construct OA- and DA-based concept discovery algorithms for encoder embedding spaces. They inherit the theoretical identifiability guarantees without requiring distributional assumptions. (4) We test them (i) on the aforementioned correlated disentanglement setting [43], (ii) on multiple and strong correlations, (iii) on discriminative encoders, and (iv) on the real-world CUB-200-2011 dataset [45]. Our approaches show increased performance against state-of-the-art disentanglement approaches, even when they are combined with post-hoc ICA.

2 RELATED WORK

From the multitude of works conducted on the identification and interpretation of components in latent spaces, our work is motivated by conceptual explanations but technically closest to the domains of disentanglement learning and ICA. We briefly review these domains in the following paragraphs.

Concept discovery for explainable AI. Recently, conceptual explanations [27, 24, 12, 48, 1] have gained popularity within the XAI community. They constitute a novel explanation technique that aims to explain a trained machine learning model post-hoc in terms of human-friendly, high-level concept directions [24]. These concepts are found via

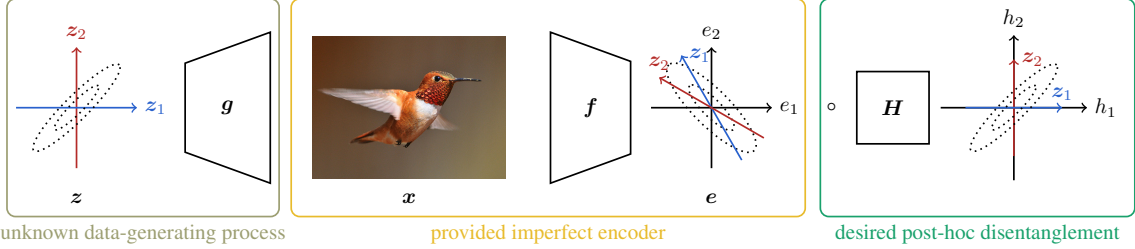


Figure 2: The decoder-encoder setup linking the latent concepts (left) to the embedding space of the provided trained model (center). A post-hoc disentanglement allows re-identifying the original concepts (right).

supervised [27, 25, 22] or unsupervised approaches [12, 48, 1, 35]. However, there are no theoretical guarantees for identifiability and the results are not always meaningful [29, 48]. Our approach can be used for unsupervised concept discovery and has a formal guarantee on identifiability rooted in disentanglement learning.

Disentanglement and ICA. The goal of disentanglement learning is finding a data-generating mechanism $g(z)$ and a latent representation z for a dataset, such that each of the original components (also known as factors of variation) is mapped to one (controllable) unit direction in z [4]. An alternative definition relies on group theory [17] where certain group operations (symmetries) should be reflected in the learned representation [33, 47]. Most works in the domain enhance VAEs [26] with additional loss terms [17, 8, 25, 9, 28]. ICA [10, 20, 19] or blind source separation (BSS) view $g(z)$ as a mixture to undo and rely on traces that the distributions over z leave in the mixture. Both domains require independence of the underlying components, which is often not applicable in naturally correlated processes. This fundamental problem was only recently shown by Träuble et al. [43] to break current disentanglement learning approaches. Hence, we design a distribution-agnostic method that is applicable even in correlated settings and outside VAEs.

Identifiability results. It has been previously shown that unsupervised disentanglement, without further assumptions, is impossible [20, 30]. Hence, recent works aim to understand the assumptions sufficient for identifiability. One strain of work relies on additional supervision, i.e., access to an additional observed variable [21, 23] or to tuples of observations that differ in only a limited number of components [31]. Another strain of work is fully unsupervised, but places distributional assumptions similar to ICA: Horan et al. [18] showed that non-Gaussian distributed, independent components, along with an isometry assumption, suffice to identify a disentangled representation. Recently, Gresele et al. [15] and Zheng et al. [49] proved identifiable disentanglement under independently distributed components and introduce a functional assumption on the data generator. Besides the distributional limitations, the above works are concerned with the generator functions but not encoders, e.g., from contrastive or discriminative tasks. Our work builds upon the recent functional independence approach and a relaxed form of an isometry assumption to proof identifiability of component directions for encoder-only setups, without independence or non-Gaussianity assumptions.

3 IDENTIFIABLE CONCEPT DISCOVERY

In this section, we identify distribution-agnostic traces that permit concept discovery methods to identify disentangled components. After formalizing the problem (Sec. 3.1), we prove that functional properties of the data-generating process leave traces in the encoder (Sec. 3.2). This allows transferring two functional properties from different origins: One stems from visual compositionality (Sec. 3.3) and one from causality principles in disentanglement learning (Sec. 3.4). We prove that both identify disentangled components and derive corresponding concept discovery algorithms.

3.1 Problem Formalization

Let us first formalize the problem setup visualized in Fig. 2. Let there be K ground-truth components whose scores are stored in $z \in \mathcal{Z} \subset \mathbb{R}^K$. Let there further be an unknown function $g : \mathcal{Z} \rightarrow \mathcal{X}$ that generates images $x = g(z) \in \mathcal{X} \subset \mathbb{R}^L$ from the components z , where $L \gg K$. Let there be a known encoder $f : \mathcal{X} \rightarrow \mathcal{E}$ that we want to scrutinize, where $e = f(x) \in \mathcal{E} \subset \mathbb{R}^K$ is the embedding of each image. We suppose that f is differentiable, so that Jacobians $J_f(x)$ exist, at least for all $x \in \{g(z) | z \in \mathcal{Z}\}$.

In the interpretability literature, concepts are frequently represented as directions in the embedding space [24, 48]. This is based on the common observation that interpretable components tend to be linearly encoded [42, 3, 2, 5]. Therefore, we suppose each ground-truth component z_i is aligned with an unknown direction $d_i \in \mathbb{R}^K$ in the embedding space.

That is, $\mathbf{e} = \mathbf{f}(g(\mathbf{z})) = \mathbf{D}\mathbf{z}$, where $\mathbf{D} = [d_1, \dots, d_K] \in \mathbb{R}^{K \times K}$. As a shorthand, we write $\mathbf{f} \circ g = \mathbf{D}$. A linear operation $\mathbf{M} \in \mathbb{R}^{K \times K}$ is said to *disentangle* the original concepts if it undoes the effect of \mathbf{D} , i.e., after applying it to the embeddings, each dimension of $\mathbf{M}\mathbf{e}$ corresponds to a component dimension in \mathbf{z} . This formally means that $\mathbf{M}\mathbf{f} \circ g = \mathbf{P}\mathbf{S}$, where $\mathbf{P} \in \mathbb{R}^{K \times K}$ is a permutation matrix that has one 1 per row and column and is otherwise 0, and $\mathbf{S} \in \mathbb{R}^{K \times K}$ is a diagonal scaling matrix.

We seek a method that provably delivers \mathbf{M} , i.e., that *identifies* it among all possible operations $\mathbf{H} \in \mathbb{R}^{K \times K}$. Besides just the embeddings $\{\mathbf{e}_n\}_{n=1,\dots,N}$, we also provide this method the N images $\{\mathbf{x}_n\}_{n=1,\dots,N}$ and the (imperfect) encoder \mathbf{f} . This task is similar to a linear ICA problem on the mixture $\mathbf{f} \circ g$, but there are some distinctive characteristics to visual embedding spaces that render the problem unidentifiable by existing approaches:

1. The distribution $p(\mathbf{z})$ is unconstrained. *Inter alia*, the components may be correlated and Gaussian.
2. g is an unknown image-generating function “of nature” and we will not approximate it.
3. Both g and \mathbf{f} are non-linear functions.
4. Our approach is unsupervised in terms of \mathbf{z} .

3.2 Transferring Functional Properties

In the outlined scenario, we will leverage functional “traces”, i.e., properties of the encoder \mathbf{f} imprinted into it through the form of the generative process, that allow disentangling the original components. Let us first define how an ideal disentangled encoder \mathbf{f}^* would look like.

Definition 3.1 (Minimal disentangled encoder (MDE)). *Let g be fixed. $\mathbf{f}^* : \mathcal{X} \rightarrow \mathcal{E}$ is a minimal disentangled encoder (MDE) of g if:*

1. $\mathbf{f}^* \circ g = \mathbf{P}\mathbf{S}$, where $\mathbf{P} \in \mathbb{R}^{K \times K}$ is a permutation and $\mathbf{S} \in \mathbb{R}^{K \times K}$ is a scaling matrix.²
2. \mathbf{f}^* has minimal total variation (min TV) within $\mathfrak{F} := \{\mathbf{f} \mid \mathbf{f} \circ g = \mathbf{P}\mathbf{S}\}$ [6].

The principle of total variation [36] and the variant for vectorized functions that we use [6] stem from classical computer vision. It constrains the norm of the gradients to be minimal and can be seen a technical condition for the upcoming proofs. Intuitively, it ensures that \mathbf{f}^* does not rely on component-unrelated information, such as noise, in the high-dimensional image space ($L \gg K$).

We want to define functional properties that g has in visual settings. But since we only suppose access to the encoder, we first need a way to transfer these properties to \mathbf{f}^* . This is done by the following lemma. It shows that if \mathbf{f}^* is an MDE of g , they must share the structure of their Jacobians.

Lemma 3.1 (Transfer lemma). *Let g be fixed and let \mathbf{f}^* be an MDE of g , where both Jacobians $\mathbf{J}_{\mathbf{f}^*}(g(\mathbf{z})) \in \mathbb{R}^{K \times L}$ and $\mathbf{J}_g(\mathbf{z}) \in \mathbb{R}^{L \times K}$ exist $\forall \mathbf{z} \in \mathcal{Z}$. Then, $\mathbf{J}_{\mathbf{f}^*}(g(\mathbf{z})) = \mathbf{P}\mathbf{S}\mathbf{J}_g(\mathbf{z})^\top \forall \mathbf{z} \in \mathcal{Z}$, where $\mathbf{P} \in \mathbb{R}^{K \times K}$ is a permutation and $\mathbf{S} \in \mathbb{R}^{K \times K}$ is a diagonal matrix.*

Proof idea. Since $\mathbf{f}^* \circ g = \mathbf{P}\mathbf{S}$, the Jacobians behave analogously. Further, the min TV condition of \mathbf{f}^* prevents $\mathbf{J}_{\mathbf{f}^*}$ from containing kernel elements of \mathbf{J}_g . The detailed proof is in Appendix B.1. \square

3.3 Concept Discovery via Disjoint Mechanisms

The transfer lemma allows any characteristic property defined in terms of the Jacobian of g to be turned into a trace when searching for \mathbf{f}^* . One possible property of visual tasks is compositionality [32]. An image comprises several parts, e.g., a bird’s wings, legs, and head, that are each controlled by one original component. Their attributions, that show the most-influenced regions and are stored in the Jacobian, should thus point to different pixels. The pixels a component affects may differ between images; the components do not need to be at the same locations and have the same size. This can be formalized as the *disjoint mechanisms* principle.

Definition 3.2 (Disjoint mechanisms (DMA)). *g is said to generate \mathbf{x} from its components \mathbf{z} via disjoint mechanisms if the Jacobian $\mathbf{J}_g(\mathbf{z})$ exists and is a block matrix $\forall \mathbf{z} \in \mathcal{Z}$. That is, the columns of $\mathbf{J}_g(\mathbf{z})$ are non-zero at disjoint rows, i.e. $|\mathbf{J}_g(\mathbf{z})|^\top |\mathbf{J}_g(\mathbf{z})| = \mathbf{S}(\mathbf{z})$, where $\mathbf{S} \in \mathbb{R}^{K \times K}$ is a diagonal matrix that may be different for each \mathbf{z} and $|\cdot|$ takes the element-wise absolute value.*

The transfer lemma allows to directly transfer this functional characteristic of g to an MDE encoder \mathbf{f}^* .

²To simplify notation, \mathbf{P} and \mathbf{S} mean *any* permutation and scale matrices. They do not have to be equal between the theorems.

Corollary 3.1 (Disjoint attributions (DA)). *If g adheres to DMA, then the rows of the Jacobian $\mathbf{J}_{f^*}(g(z))$ of any MDE f^* must be disjoint $\forall z \in \mathcal{Z}$, that is, $|\mathbf{J}_{f^*}(g(z))||\mathbf{J}_{f^*}(g(z))^\top| = \mathbf{S}(z)$, where $\mathbf{S} \in \mathbb{R}^{K \times K}$ is a diagonal matrix that may be different for each z and $|\cdot|$ takes element-wise absolute values.*

Now, we have a characteristic trace at hand that an MDE f^* necessarily fulfills. The following theorem shows that it is also a sufficient property, i.e., only MDEs fulfill it.

Theorem 3.1 (Identifiability under DMA). *Let g adhere to DMA. Let f be given with $f \circ g = \mathbf{D}$, where both $\mathbf{J}_{f^*}(g(z))$ and $\mathbf{J}_g(z)$ exist $\forall z \in \mathcal{Z}$. If there exists an MDE $f^* = \mathbf{M}f$, where $\mathbf{M} \in \mathbb{R}^{K \times K}$ has full rank, then an $f' = \mathbf{H}f$ with a full-rank $\mathbf{H} \in \mathbb{R}^{K \times K}$ and disjoint rows in its Jacobian $\mathbf{J}_{f'}(g(z))$ for some $z \in \mathcal{Z}$ must be an MDE.*

Proof idea. Corollary 3.1 yields that an MDE $\mathbf{M}f$ of a DMA process must have disjoint rows in its Jacobian. In fact, only permutations and scales of \mathbf{M} can have this property. This includes the given \mathbf{H} . So, $\mathbf{H}f$ must be an MDE. Note that as $\mathbf{H}f$ is an MDE of a DMA process, it will also have disjoint rows in its Jacobians across all $z \in \mathcal{Z}$. The detailed proof is in Appendix B.3. \square

Thus, we can identify a disentangled \mathbf{M} by checking which \mathbf{H} leads to a $\mathbf{H}f$ with DA. The proof can even be turned into an analytical solution for \mathbf{H} . We discuss this concept discovery strategy in Appendix B.5. Alternatively, we can minimize a loss function that computes the overall degree of non-disjointness of $\mathbf{H}f$ to find a suitable \mathbf{H} :

$$\mathcal{L}(\mathbf{H}) = \mathbb{E}_{\mathbf{x}} \|\text{arn}[\mathbf{H}\mathbf{J}_f(\mathbf{x})] \text{arn}[\mathbf{H}\mathbf{J}_f(\mathbf{x})]^\top - \mathbf{I}\|_F^2. \quad (1)$$

The expectation is taken over a collection of real data samples \mathbf{x} . The arn-operator (absolute values, row normalization) takes the element-wise absolute value and subsequently effects a row-wise normalization. This is done to not constrain the norms of the Jacobian's rows but only enforces disjointness. This objective can be optimized via off-the-shelf stochastic gradient descent (SGD).

3.4 Concept Discovery via Independent Mechanisms

With the versatile transfer lemma in place, we have the means to also investigate different classes of processes. Grounded by causal principles instead of compositionality, the independent mechanisms property has been argued to define a class of natural generators [15].

Definition 3.3 (Independent mechanisms (IMA)). *g is said to generate \mathbf{x} from its components z via independent mechanisms if the Jacobian $\mathbf{J}_g(z)$ of g exists and its columns (one per component) are orthogonal $\forall z \in \mathcal{Z}$, i.e., $\mathbf{J}_g^\top(z)\mathbf{J}_g(z) = \mathbf{S}(z)$, where $\mathbf{S} \in \mathbb{R}^{K \times K}$ is a diagonal matrix that may differ for each z [15].*

Gresele et al. [15] and Zheng et al. [49] used this characteristic only to find disentangled generators, but the transfer lemma allows to turn it into a trace that the MDE f^* has to fulfill. This makes it applicable to post-hoc disentanglement of learned encoders.

Corollary 3.2 (Orthogonal attributions (OA)). *If g adheres to IMA, then the Jacobian $\mathbf{J}_{f^*}(g(z))$ of any MDE f^* must have orthogonal rows $\forall z \in \mathcal{Z}$, that is, $\mathbf{J}_{f^*}(g(z))\mathbf{J}_{f^*}(g(z))^\top = \Sigma(z)$, where $\Sigma(z) \in \mathbb{R}^{K \times K}$ is a diagonal matrix that may be different for each z .*

We now have an alternative trace to search for in case the data generating process does not fulfill DMA, but only confirms to the weaker IMA condition. However it is no more strong enough to ensure identifiability in the most general case, since it is invariant to certain rotations. This is prevented under an additional technical condition on $\Sigma(z)$, which we refer to as *non-equal magnitude ratios* (NEMR). Intuitively, it requires that the magnitudes of the component gradients change non-uniformly between at least two points.

Theorem 3.2 (Identifiability under IMA). *Let g adhere to IMA. Let f be given with $f \circ g = \mathbf{D}$, where both $\mathbf{J}_f(g(z))$ and $\mathbf{J}_g(z)$ exist $\forall z \in \mathcal{Z}$. Suppose there exists an MDE $f^* = \mathbf{M}f$, where $\mathbf{M} \in \mathbb{R}^{K \times K}$ has full rank. Suppose we have obtained an $f' = \mathbf{H}f$ with a full-rank $\mathbf{H} \in \mathbb{R}^{K \times K}$ and orthogonal rows in its Jacobian $\mathbf{J}_{f'}(g(z))$ for two points $z_a, z_b \in \mathcal{Z}$. If z_a and z_b fulfill $\gamma_i := \frac{\Sigma_{ii}(z_b)}{\Sigma_{ii}(z_a)}$ and $\forall i, j = 1 \dots K, i \neq j : \gamma_i \neq \gamma_j$ (NEMR condition), then \mathbf{H} must be a permuted, scaled version of \mathbf{M} , $\mathbf{H} = \mathbf{S}\mathbf{P}\mathbf{M}$, where $\mathbf{P} \in \mathbb{R}^{K \times K}$ is an permutation and $\mathbf{S} \in \mathbb{R}^{K \times K}$ is a diagonal scaling matrix. Thus, f' is an MDE.*

The detailed proof is given in Appendix B.4. \square

This constructive proof can also be condensed into an analytical solution that relies on eigenvalue decompositions. Alternatively, one can again construct a suitable optimization objective. This is achieved by removing the absolute value operation from the arn-operator in Eqn. (1), so that it solely performs a row-wise normalization.

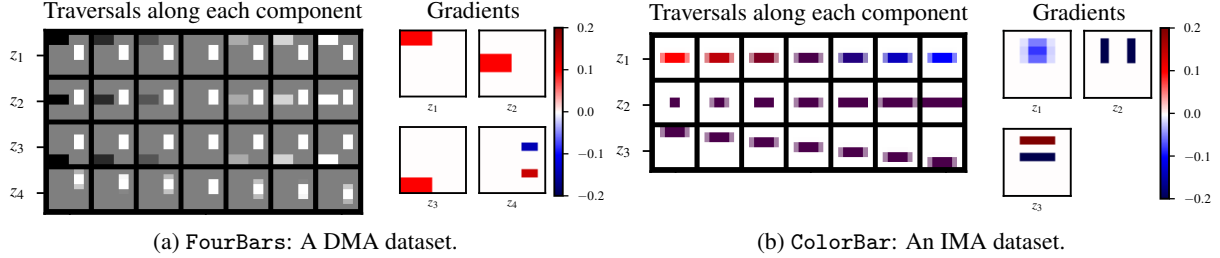


Figure 3: The two synthetic datasets. Their gradients for an example image are solved in closed-form (right to traversals), showing that their J_g fulfill DMA (a) and IMA (b).

4 EXPERIMENTS

In the following, we perform benchmarks of increasing complexity to compare the practical capabilities of DA and OA. We start by verifying the theoretical identifiability conditions (Sec. 4.1), then perform disentanglement benchmarks under increasing multi-component correlations (Sec. 4.2 to 4.4), and finally make an initial attempt on a large-scale, discriminatively-trained ResNet50 encoder (Sec. 4.5).

We report the DCI [11] implemented in the `disentanglement.lib` [30] to measure whether each discovered component predicts precisely one ground-truth component and vice versa. Following Locatello et al. [31], we report additional metrics with similar results (FactorVAE [25], SAP [28], MIG [9]) in the appendix, along with results on additional datasets and ablations. For reproducibility, each experiment is repeated on five seeds and code is made available upon acceptance. In total, we train and disentangle over 300 embedding spaces, requiring about 124 Nvidia RTX2080Ti GPU days. More implementation details can be found in Appendix C.

4.1 Confirming Identifiability Conditions

We first demonstrate the analytical solutions and thereby confirm our identifiability guarantees. We implement two realistic synthetic datasets with differentiable generators. This allows computing the closed-form of J_g and deliberately fulfilling or violating the DMA, IMA, and NEMR conditions.

FourBars consists of gray-scale images of four components: Three bars change their colors (black to white) and one bar moves vertically, showing that the image regions affected by each component may change in each image. The plot of J_g in Fig. 3a shows that each component maps to a disjoint image region. This fulfills DMA and thus also IMA. However, all factors have the same gradient magnitudes, making it impossible to find two points with NEMR. According to the proofs, we expect DA to work and OA to fail. The second dataset, ColorBar, contains a single bar that undergoes realistic changes in color, width, and its vertical position, see Fig. 3b. It conforms to IMA and NEMR but not DMA. Our proofs indicate that OA should work and DA fail. Completing the problem formalization in Sec. 3.1, we compute analytical MDEs f^* for these datasets and distort them by multiplication with a random matrix D .

On FourBars, the analytical solution of DA indeed delivers an H that perfectly disentangles the components (DCI=1.00 ± 0.00) while OA fails (DCI=0.24 ± 0.10). On ColorBars, OA delivers perfect disentanglement (DCI=1.00 ± 0.00) whereas DA fails (DCI=0.26 ± 0.05). This aligns with our theory and shows the capability to disentangle visual embeddings based on Jacobians alone, while contrasting the nuanced identifiability conditions.

4.2 Embedding Spaces with Correlated Components

We now move to the common Shapes3D [7] visual disentanglement benchmark dataset. It shows geometric bodies that vary in their colors, shape, orientation, size, and background totaling six components. Compared to the previous section, the components in this dataset are more complex and we correlate them: Following Träuble et al. [43], the dataset is resampled such that two components $z_i, z_j \in [0, 1]$ follow $z_i - z_j \sim \mathcal{N}(0, s^2)$. Lower s results in a stronger correlation where only few pairs of component values co-occur frequently. We choose a moderate correlation of $s = 0.4$ here and three pairs z_i, z_j that are nominal/nominal, nominal/ordinal, and ordinal/ordinal variables. We train four state-of-the-art disentanglement learning VAEs (BetaVAE [17], FactorVAE [25], BetaTCVAE [9], DipVAE [28]) from a recent study [30] and apply ICA, PCA, and our DA and OA methods on their embedding spaces to post-hoc discover the original components. For DA and OA, we use the optimization-based algorithms that iterate over the

Correlated components	floor & background	orientation & background	orientation & size
BetaVAE	0.497 ± 0.028	0.581 ± 0.044	0.491 ± 0.049
+PCA	0.263 ± 0.028	0.310 ± 0.025	0.324 ± 0.041
+ICA	0.574 ± 0.040	0.540 ± 0.080	0.577 ± 0.038
+Ours (OA)	0.617 ± 0.018	0.602 ± 0.050	0.579 ± 0.032
+Ours (DA)	0.641 ± 0.031	0.624 ± 0.055	0.627 ± 0.031
FactorVAE	0.507 ± 0.105	0.502 ± 0.076	0.712 ± 0.010
+PCA	0.358 ± 0.075	0.474 ± 0.051	0.556 ± 0.029
+ICA	0.294 ± 0.070	0.263 ± 0.053	0.340 ± 0.034
+Ours (OA)	0.551 ± 0.040	0.498 ± 0.034	0.595 ± 0.051
+Ours (DA)	0.584 ± 0.047	0.510 ± 0.055	0.556 ± 0.038
BetaTCVAE	0.619 ± 0.008	0.613 ± 0.041	0.659 ± 0.005
+PCA	0.400 ± 0.030	0.421 ± 0.068	0.450 ± 0.065
+ICA	0.540 ± 0.023	0.497 ± 0.036	0.627 ± 0.023
+Ours (OA)	0.623 ± 0.021	0.652 ± 0.028	0.638 ± 0.037
+Ours (DA)	0.666 ± 0.010	0.664 ± 0.023	0.748 ± 0.026
DipVAE	0.631 ± 0.018	0.652 ± 0.017	0.548 ± 0.036
+PCA	0.158 ± 0.013	0.160 ± 0.020	0.170 ± 0.022
+ICA	0.630 ± 0.018	0.651 ± 0.017	0.542 ± 0.033
+Ours (OA)	0.644 ± 0.019	0.624 ± 0.014	0.558 ± 0.051
+Ours (DA)	0.684 ± 0.009	0.679 ± 0.013	0.601 ± 0.055

Table 1: Mean \pm std. err. of the DCI scores (across all components of Shapes3D) of several models and post-hoc methods applied to their embeddings. Columns show which pair of components was correlated during training.

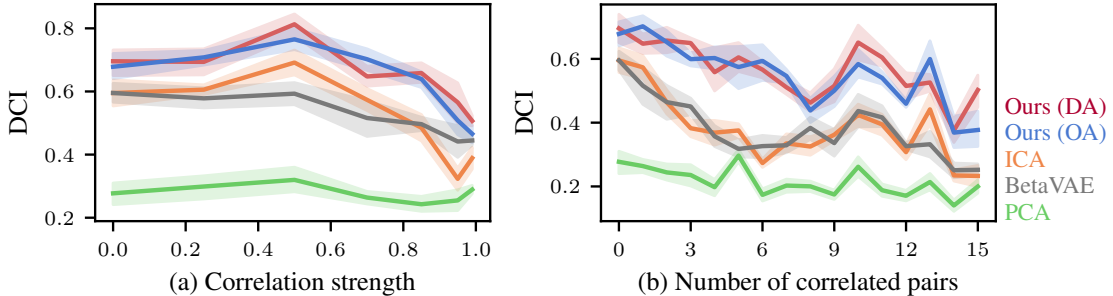


Figure 4: Robustness under Gaussian prior and increasing pairwise correlations between concepts. Shaded areas show the standard deviation of the mean over five seeds. Best viewed in color.

whole dataset instead of only two samples, since they appear more robust to the noisy gradient estimates (cf. Tab. 5 in the Appendix).

Sec. 4.2 shows the resulting DCI scores. In line with Träuble et al. [43], we find that the disentanglement learning VAEs fail to disentangle the correlated components on their own due to their violated stochastic independence assumption. In eleven of the twelve setups, DA/OA identify better entangled components than the VAE unit axes and the than PCA/ICA components, impressively highlighting that their concept discovery works regardless of the embedding space and the type of components correlated. On average, DA delivers better results than OA (+0.047), despite Shapes3D violating the DMA assumption. This indicates that the DA objective’s loss might be more robustly optimizable in practice. Fig. 1 visualizes the disentanglement achieved via DA as a traversal plot and also shows that small DCI differences can mean a big improvement in disentanglement, because the metric is computed across all components but only two components are correlated. We investigate other correlation strengths with similar findings in Appendix D.3.

We conduct further experiments on the challenging MPI3D-real [13] dataset in Appendix D.2. Here, the VAEs struggle to reconstruct the fine-detailed images, let alone disentangle the components. However, DA works well with the DipVAE model, and OA still leads to improvement for the BetaVAE model, while PCA and ICA consistently fail to beat either the VAE unit axes or OA/DA. Unlike on Shapes3D, we observed no substantial performance gap between OA and DA on MPI3D-real.

4.3 Gaussianity and Multiple Correlations

In this section, we increase the distributional challenges to analyze whether our approaches are as distribution-agnostic as intended. We sample the components of Shapes3D from a (rotationally-symmetric) Gaussian. Additionally, we introduce correlations between multiple components to its covariance matrix. Technical details on how singular covariance matrices are prevented are given in Appendix C.3.

First, we study a single pair of correlated components (floor and background color) with increasing correlation strength ρ . Fig. 4 shows that the BetaVAE handles low correlations well but starts deteriorating from a strength of $\rho > 0.5$, along with ICA. The DCI of our methods is an average constant of $+0.145$ above the BetaVAE’s for $\rho \leq 0.85$. After this, it returns to the underlying BetaVAE’s DCI, possibly because the two components collapsed in the BetaVAE’s embedding space. For Fig. 4b, we gradually add more moderately correlated ($\rho \approx 0.7$) pairs to the Gaussian’s covariance matrix until eventually all components are correlated. Again, our models show a constant benefit over the underlying BetaVAE’s DCI curve. This demonstrates that a post-hoc method’s performance depends on the underlying model but that it can outperform it consistently. Also, BetaVAE’s and ICA’s initial decay is faster than in the previous experiment. This reveals their struggle in settings where multiple components are correlated. In this experiment, there were no considerable differences between DA and OA.

4.4 Discriminative Latent Spaces

A key characteristic of our approach is that it can be applied to latent spaces of classification models that were trained in a purely discriminative manner, e.g., the feature space of a CNN model. To investigate this setting, we set up an 8-class classification problem on the Shapes3D dataset, where the combination of the four binarized components object color, wall color (blue/red vs. yellow/green), shape (cylinder vs. cube) and orientation (left vs. right) determines the class (cf. Appendix C.4). To make the setting even more realistic, we artificially add labeling noise close to the decision boundary, correlations as in Sec. 4.2, and an L2-regularizer on the embeddings to constrain them to a reasonable range. We train a simple CNN with a $K=6$ -dimensional embedding space before the final classification layer.

The discriminative loss leads to a clustered distribution in the embedding space. ICA expectedly works very well in this highly non-Gaussian distribution, when no significant correlations are present. However, tables turn as we increasingly correlate the floor and background color: Starting at $s = 0.2$, DA outperforms ICA and the other methods as can be seen in table Sec. 4.4. This demonstrates that our method is applicable to purely discriminative latent spaces and, in line with the previous experiment, that it is more robust to high levels of correlations than ICA. While OA leads to increased disentanglement over the unit directions, it does not reach the level of DA in this experiment.

Method	$s = 0.1$	$s = 0.15$	$s = 0.2$
unit dirs.	0.238 ± 0.01	0.244 ± 0.01	0.247 ± 0.01
PCA	0.238 ± 0.01	0.376 ± 0.03	0.373 ± 0.03
ICA	0.409 ± 0.02	0.309 ± 0.02	0.311 ± 0.01
(Ours) OA	0.295 ± 0.01	0.302 ± 0.01	0.333 ± 0.04
(Ours) DA	0.435 ± 0.01	0.411 ± 0.03	0.392 ± 0.02

Table 2: Mean \pm std. err. of the DCI scores for concept discovery in a discriminative latent space.

4.5 Real-world Concept Discovery

Last, we go beyond the traditional benchmarks and attempt a close-to-praxis concept discovery: We post-hoc disentangle a ResNet50 classifier [16] trained on the CUB-200-2011 [45] dataset consisting of high-resolution images of birds. This combines the challenges of the previous sections and scales them up, i.e., a discriminative space, non-linear component dependencies of varying strengths across multiple components, and a large 512-dimensional embedding space. One restriction of this experiment is that CUB has no data-generating components to compare against, so we cannot report DCI scores. However, we qualitatively show that DA can deliver interpretable components in this close-to-praxis setup by matching them to annotated attributes of CUB.

We apply OA and DA to discover $K=30$ components of which three are shown exemplarily in Fig. 5. The images with the highest positive scores on the first component (on the right) consistently show white birds. The other end of the component comprises birds whose primary color is black. This gives a high Spearman rank correlation with the CUB attribute “primary color: white”. The other two components are similarly interpretable. To quantify this across all K components, we provide an initial quantitative evaluation based on the Spearman rank correlation between

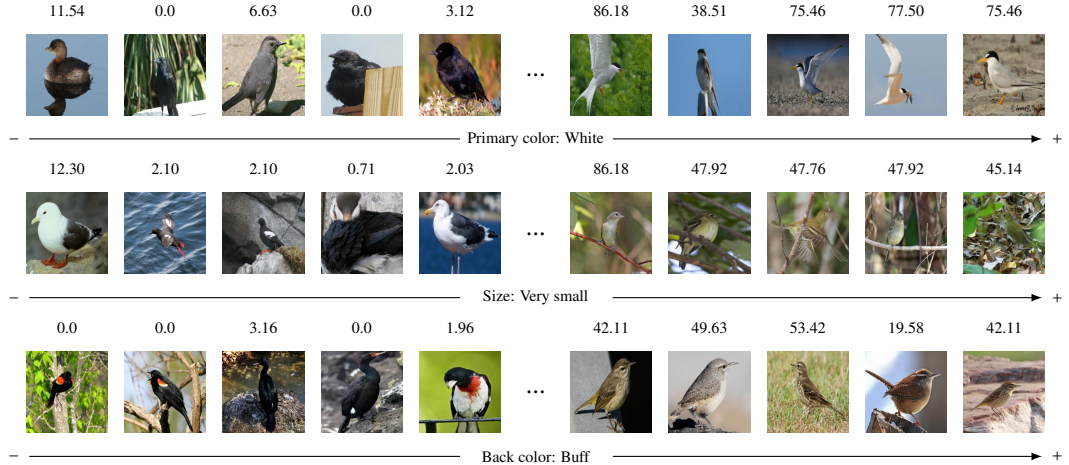


Figure 5: Three exemplary components that DA discovered on CUB, along with images that score the highest (right) and lowest (left) on them. Each component correlates with an interpretable attribute provided in CUB. The numbers on top give the ground-truth value of these attributes.

components and attributes in Appendix D.6. It indicates that ICA and PCA have problems providing such components and the components identified by DA usually correspond more closely to the attributes when compared to OA. The construction of further quantitative evaluation schemes on datasets like CUB goes beyond the scope of this work. These promising results indicate that DA can be applied to high-dimensional, real-world datasets.

5 DISCUSSION AND CONCLUSION

Summary. We derived the two functional, distribution-agnostic paradigms of disjoint and orthogonal attributions and theoretically proved that they identify disentangled components in visual embedding spaces. Our extensive experiments reveal that they both are applicable to various disentanglement learning and discriminative models and remain relatively unaffected by distributional challenges.

Disjoint vs. orthogonal attributions. Disjoint mechanisms can be derived from visual compositionality properties whereas independent mechanisms are grounded in causal principles. In theory, independent mechanisms are indisputably more general. The resulting orthogonality loss (OA) outperformed many baselines. Nevertheless, we empirically observed superior results with the disjoint loss (DA) for the complex datasets. We hypothesize that the disjoint loss is more robust to noisy gradient signals and may be easier to optimize. Our theoretic results relying on IMA may however be more broadly applicable to non-vision tasks and serve as a valuable starting point for further investigation.

Outlook. In this work, we disentangled components in given encoders in a post-hoc manner. However, the transfer lemma and corollaries 3.2 and 3.1 (disjoint and orthogonal attributions) are more general than the identifiability proofs and do not require an imperfect encoder function to be available. Therefore, the general paradigm of finding characteristic traces of the data-generating process and transferring them to construct matching encoders can be applied beyond concept discovery. This might be relevant to approaches that regularize for orthogonality criteria directly during training of the encoder. In this light, we believe the insights derived in this work can be impactful in the broader scope of learning interpretable representations.

Acknowledgments

The authors thank Frederik Träuble, Luigi Gresele, and Julius von Kügelgen for insightful discussions during the early development of this project. This work was funded by the Deutsche Forschungsgemeinschaft (DFG, German Research Foundation) under Germany’s Excellence Strategy – EXC number 2064/1 – Project number 390727645. The authors thank the International Max Planck Research School for Intelligent Systems (IMPRS-IS) for supporting Michael Kirchhof.

References

- [1] A. Akula, S. Wang, and S.-C. Zhu. Cocox: Generating conceptual and counterfactual explanations via fault-lines. In *Proceedings of the AAAI Conference on Artificial Intelligence*, volume 34, pages 2594–2601, 2020.
- [2] G. Alain and Y. Bengio. Understanding intermediate layers using linear classifier probes. *arXiv preprint arXiv:1610.01644*, 2016.
- [3] D. Bau, B. Zhou, A. Khosla, A. Oliva, and A. Torralba. Network dissection: Quantifying interpretability of deep visual representations. In *Proceedings of the IEEE conference on computer vision and pattern recognition*, pages 6541–6549, 2017.
- [4] Y. Bengio, A. Courville, and P. Vincent. Representation learning: A review and new perspectives. *IEEE transactions on pattern analysis and machine intelligence*, 35(8):1798–1828, 2013.
- [5] A. Bisazza and C. Tump. The lazy encoder: A fine-grained analysis of the role of morphology in neural machine translation. In *Proceedings of the 2018 Conference on Empirical Methods in Natural Language Processing*, pages 2871–2876. Association for Computational Linguistics, 2018.
- [6] P. Blomgren and T. F. Chan. Color tv: total variation methods for restoration of vector-valued images. *IEEE transactions on image processing*, 7(3):304–309, 1998.
- [7] C. Burgess and H. Kim. 3d shapes dataset. <https://github.com/deepmind/3dshapes-dataset/>, 2018.
- [8] C. P. Burgess, I. Higgins, A. Pal, L. Matthey, N. Watters, G. Desjardins, and A. Lerchner. Understanding disentangling in β -VAE. *arXiv preprint arXiv:1804.03599*, 2018.
- [9] R. T. Chen, X. Li, R. B. Grosse, and D. K. Duvenaud. Isolating sources of disentanglement in variational autoencoders. *Advances in neural information processing systems*, 31, 2018.
- [10] P. Comon. Independent component analysis, a new concept? *Signal processing*, 36(3):287–314, 1994.
- [11] C. Eastwood and C. K. Williams. A framework for the quantitative evaluation of disentangled representations. In *International Conference on Learning Representations*, 2018.
- [12] A. Ghorbani, J. Wexler, J. Y. Zou, and B. Kim. Towards automatic concept-based explanations. In *Advances in Neural Information Processing Systems*, volume 32, pages 9277–9286, 2019.
- [13] M. W. Gondal, M. Wuthrich, D. Miladinovic, F. Locatello, M. Breidt, V. Volchkov, J. Akpo, O. Bachem, B. Schölkopf, and S. Bauer. On the transfer of inductive bias from simulation to the real world: a new disentanglement dataset. *Advances in Neural Information Processing Systems*, 32, 2019.
- [14] I. Goodfellow, J. Pouget-Abadie, M. Mirza, B. Xu, D. Warde-Farley, S. Ozair, A. Courville, and Y. Bengio. Generative adversarial nets. *Advances in neural information processing systems*, 27, 2014.
- [15] L. Gresele, J. von Kügelgen, V. Stimper, B. Schölkopf, and M. Besserve. Independent mechanism analysis, a new concept? In *Advances in Neural Information Processing Systems*, 2021.
- [16] K. He, X. Zhang, S. Ren, and J. Sun. Deep residual learning for image recognition. In *Proceedings of the IEEE conference on computer vision and pattern recognition*, pages 770–778, 2016.
- [17] I. Higgins, L. Matthey, A. Pal, C. Burgess, X. Glorot, M. Botvinick, S. Mohamed, and A. Lerchner. beta-vae: Learning basic visual concepts with a constrained variational framework. In *International Conference on Learning Representations*, 2017.
- [18] D. Horan, E. Richardson, and Y. Weiss. When is unsupervised disentanglement possible? In *Advances in Neural Information Processing Systems*, 2021.
- [19] A. Hyvärinen, J. Karhunen, and E. Oja. *Independent component Analysis*. John Wiley & Sons, Inc, 2001.
- [20] A. Hyvärinen and P. Pajunen. Nonlinear independent component analysis: Existence and uniqueness results. *Neural Networks*, 12(3):429–439, 1999. ISSN 0893-6080.

[21] A. Hyvärinen, H. Sasaki, and R. Turner. Nonlinear ica using auxiliary variables and generalized contrastive learning. In *The 22nd International Conference on Artificial Intelligence and Statistics*, pages 859–868. PMLR, 2019.

[22] D. Kazhdan, B. Dimanov, M. Jamnik, P. Liò, and A. Weller. Now you see me (cme): concept-based model extraction. *AIMLAI workshop at the 29th ACM International Conference on Information and Knowledge Management (CIKM)*, 2020.

[23] I. Khemakhem, D. Kingma, R. Monti, and A. Hyvärinen. Variational autoencoders and nonlinear ICA: A unifying framework. In *International Conference on Artificial Intelligence and Statistics*, pages 2207–2217. PMLR, 2020.

[24] B. Kim, M. Wattenberg, J. Gilmer, C. Cai, J. Wexler, F. Viegas, et al. Interpretability beyond feature attribution: Quantitative testing with concept activation vectors (tcav). In *International Conference on Machine Learning*, pages 2668–2677. PMLR, 2018.

[25] H. Kim and A. Mnih. Disentangling by factorising. In *International Conference on Machine Learning*, pages 2649–2658. PMLR, 2018.

[26] D. P. Kingma and M. Welling. Auto-encoding variational bayes. *arXiv preprint arXiv:1312.6114*, 2013.

[27] P. W. Koh, T. Nguyen, Y. S. Tang, S. Mussmann, E. Pierson, B. Kim, and P. Liang. Concept bottleneck models. In *International Conference on Machine Learning*, pages 5338–5348. PMLR, 2020.

[28] A. Kumar, P. Sattigeri, and A. Balakrishnan. Variational inference of disentangled latent concepts from unlabeled observations. In *International Conference on Learning Representations*, 2018.

[29] T. Leemann, Y. Rong, S. Kraft, E. Kasneci, and G. Kasneci. Coherence evaluation of visual concepts with objects and language. In *ICLR2022 Workshop on the Elements of Reasoning: Objects, Structure and Causality*, 2022.

[30] F. Locatello, S. Bauer, M. Lucic, G. Raetsch, S. Gelly, B. Schölkopf, and O. Bachem. Challenging common assumptions in the unsupervised learning of disentangled representations. In *International Conference on Machine Learning*, pages 4114–4124. PMLR, 2019.

[31] F. Locatello, B. Poole, G. Rätsch, B. Schölkopf, O. Bachem, and M. Tschannen. Weakly-supervised disentanglement without compromises. In *International Conference on Machine Learning*, pages 6348–6359. PMLR, 2020.

[32] B. Ommer and J. M. Buhmann. Learning the compositional nature of visual objects. In *2007 IEEE Conference on Computer Vision and Pattern Recognition*, 2007.

[33] M. Painter, A. Prugel-Bennett, and J. Hare. Linear disentangled representations and unsupervised action estimation. In *Advances in Neural Information Processing Systems*, volume 33, pages 13297–13307. Curran Associates, Inc., 2020.

[34] A. Ramesh, Y. Choi, and Y. LeCun. A spectral regularizer for unsupervised disentanglement. *arXiv preprint arXiv:1812.01161*, 2018.

[35] X. Ren, T. Yang, Y. Wang, and W. Zeng. Learning disentangled representation by exploiting pretrained generative models: A contrastive learning view. In *International Conference on Learning Representations*, 2022.

[36] L. I. Rudin, S. Osher, and E. Fatemi. Nonlinear total variation based noise removal algorithms. *Physica D: nonlinear phenomena*, 60(1-4):259–268, 1992.

[37] A. Sepliarskaia, J. Kiseleva, M. de Rijke, et al. Evaluating disentangled representations. *arXiv preprint arXiv:1910.05587*, 2019.

[38] H. Shah, P. Jain, and P. Netrapalli. Do input gradients highlight discriminative features? In M. Ranzato, A. Beygelzimer, Y. Dauphin, P. Liang, and J. W. Vaughan, editors, *Advances in Neural Information Processing Systems*, volume 34, pages 2046–2059, 2021. URL <https://proceedings.neurips.cc/paper/2021/file/0fe6a94848e5c68a54010b61b3e94b0e-Paper.pdf>.

[39] K. Simonyan, A. Vedaldi, and A. Zisserman. Deep inside convolutional networks: Visualising image classification models and saliency maps. *arXiv preprint arXiv:1312.6034*, 2013.

[40] D. Smilkov, N. Thorat, B. Kim, F. Viégas, and M. Wattenberg. Smoothgrad: removing noise by adding noise. In *Workshop on Visualization for Deep Learning, ICML*, 2017.

[41] M. Sundararajan, A. Taly, and Q. Yan. Axiomatic attribution for deep networks. In *International Conference on Machine Learning*, pages 3319–3328. PMLR, 2017.

[42] C. Szegedy, W. Zaremba, I. Sutskever, J. Bruna, D. Erhan, I. Goodfellow, and R. Fergus. Intriguing properties of neural networks. *arXiv preprint arXiv:1312.6199*, 2013.

- [43] F. Träuble, E. Creager, N. Kilbertus, F. Locatello, A. Dittadi, A. Goyal, B. Schölkopf, and S. Bauer. On disentangled representations learned from correlated data. In *International Conference on Machine Learning*, pages 10401–10412. PMLR, 2021.
- [44] A. Voynov and A. Babenko. Unsupervised discovery of interpretable directions in the gan latent space. In *International Conference on Machine Learning*, pages 9786–9796. PMLR, 2020.
- [45] C. Wah, S. Branson, P. Welinder, P. Perona, and S. Belongie. The Caltech-UCSD Birds-200-2011 Dataset. Technical Report CNS-TR-2011-001, 2011.
- [46] Y. Wei, Y. Shi, X. Liu, Z. Ji, Y. Gao, Z. Wu, and W. Zuo. Orthogonal jacobian regularization for unsupervised disentanglement in image generation. In *Proceedings of the IEEE/CVF International Conference on Computer Vision*, pages 6721–6730, 2021.
- [47] T. Yang, X. Ren, Y. Wang, W. Zeng, and N. Zheng. Towards building a group-based unsupervised representation disentanglement framework. In *International Conference on Learning Representations*, 2021.
- [48] C.-K. Yeh, B. Kim, S. O. Arik, C.-L. Li, T. Pfister, and P. Ravikumar. On completeness-aware concept-based explanations in deep neural networks. In *Advances in Neural Information Processing Systems*, volume 32, 2019.
- [49] Y. Zheng, I. Ng, and K. Zhang. On the identifiability of nonlinear ICA with unconditional priors. In *ICLR2022 Workshop on the Elements of Reasoning: Objects, Structure and Causality*, 2022.

A Additional Related Work

Orthogonality constraints and disentanglement for generative models. In the context of generative adversarial networks (GANs) [14], the problem of analyzing and discovering interpretable directions has been studied recently by Voynov and Babenko [44]. Ren et al. [35] propose a contrastive approach to discover interpretable directions using pretrained generative models. Wei et al. [46] have proposed an orthogonality regularization of the Jacobian, which resulted in more interpretable generative abilities. Ramesh et al. [34] constrain the right-singular vectors of a generator Jacobian to be unit directions, which corresponds to column-wise orthogonal generator Jacobians. We go beyond these works, by providing rigorous results on identifiability and by extending the scope to a much broader class of models.

B Proofs

B.1 Transfer lemma

Let $z \in \mathcal{Z}$ be arbitrary. Since $(f^* \circ g)(z) = PSz$, it must be that $J_{f^*}(g(z))J_g(z) = PS$.

Now, let us write $J_{f^*}(g(z)) = [v_1, \dots, v_K]^\top$ with $v_i \in \mathbb{R}^L$. Similarly, we can write $J_g(z) = [w_1, \dots, w_K]$ with $w_i \in \mathbb{R}^L$, $i = 1, \dots, K$, and $S = \text{diag}(\alpha_1, \dots, \alpha_K)$ with $\alpha_k \in \mathbb{R}_{\neq 0}$, $k = 1, \dots, K$.

Let us focus on an individual row of J_{f^*} , i.e., let $k \in \{1, \dots, K\}$ be a fixed index of a row. Since $J_{f^*}(z)J_g(z) = PS$ and P is a permutation matrix with exactly one 1 per row, there is precisely one column index k' such that the k -th row and k' -th column of PS is non-zero. This setup allows drawing certain conclusions about the vector v_k . Let $j = 1, \dots, K$ denote an arbitrary column of PS . Then,

(i) if $j = k'$, then $v_k^\top w_{k'} = \alpha_{k'} \neq 0$. In consequence, $v_k \neq 0$, $w_{k'} \neq 0$ and so we can decompose $v_k = a_k + b_k$, where $a_k \in \text{span}(\{w_{k'}\}) \setminus \{0\}$ and $b_k \in \text{span}(\{w_{k'}\})^\perp$, where \perp denotes the orthogonal complement. Because $\text{span}(\{w_{k'}\}) = \{\mu w_{k'} | \mu \in \mathbb{R}\}$, we know that $a_k = \frac{\alpha_{k'}}{\|w_{k'}\|_2^2} w_{k'}$.

(ii) if $j \neq k'$, then $v_k^\top w_j = 0$. With (i), it follows that $b_k \in \text{span}(\{w_1, \dots, w_K\})^\perp = \ker(J_g^\top(z))$.

So, we know that each row of J_{f^*} must correspond to a (scaled) column of J_g , plus possibly an element of the kernel of the columns of J_g . What is left to prove is that this kernel element is zero due to the min TV property, i.e., $b_k = 0$.

The principle of total variation for vector-valued function that f^* fulfills states (point-wisely evaluated) that $\|J_{f^*}\|_F$ should be minimal. $\sqrt{\|J_{f^*}\|_F^2} = \sqrt{\sum_{k=1}^K \|a_k + b_k\|_2^2} = \sqrt{\sum_{k=1}^K \|a_k\|_2^2 + \|b_k\|_2^2}$, due to the orthogonality of a_k and b_k . The unique solution for minimizing this expression that maintains $f^* \circ g = PS$ (that means fulfilling (i) and (ii)) is $b_k = 0$, $\forall k = 1, \dots, K$. Hence, $v_k = a_k + 0 = \frac{\alpha_{k'}}{\|w_{k'}\|_2^2} w_{k'} + 0$ for our selected row k . Globally, this means $J_{f^*}(g(z)) = P' S' J_g(z)^\top$, with some scaling matrix S' and permutation matrix P' . \square

B.2 Preliminaries

We start by first proving an auxiliary lemma. We show that orthogonality of Jacobians, i.e., $J_f J_f^\top = S$ with a diagonal matrix S will be destroyed in the general case when a rotation R is applied, such that $J_{Rf} J_{Rf}^\top = R J_f J_f^\top R^\top = R S R^\top$ is not a diagonal matrix anymore.

Lemma B.1 (Rotations destroy orthogonality patterns.). *Let $S \in \mathbb{R}^{K \times K}$ be a diagonal matrix, $S = \text{diag}(s)$ with diagonal entries $s > 0$ and $s_i \neq s_j$, $\forall i \neq j$, i.e., all diagonal entries of S are different and positive. Let $R \in \mathbb{R}^{K \times K}$ be any rotation matrix with $R^\top R = I$. If $R S R^\top$ is a diagonal matrix, R must be a signed permutation matrix (a permutation matrix where entries can be ± 1).*

Proof. With $R S R^\top = \text{diag}(\lambda_1, \dots, \lambda_K)$, we have for each unit vector $e^{(i)}$, $i = 1, \dots, K$, that

$$R S R^\top e^{(i)} = \lambda_i e^{(i)}. \quad (2)$$

We can represent R by its rows, $R = [r_1, \dots, r_K]^\top$ where each $r_i \in \mathbb{R}^K$. In this notation, $R^\top e^{(i)} = r_i$, i.e., multiplication of the transpose with a unit vector will select the row r_i . This results in

$$R S r_i = \lambda_i e^{(i)} \quad (3)$$

Because R is invertible and square, we can left-multiply the equation by R^\top . Using $R^\top e^{(i)} = r_i$ again, we arrive at

$$S r_i = \lambda_i r_i. \quad (4)$$

This implies that all \mathbf{r}_i are eigenvectors of the matrix \mathbf{S} with the eigenvalues λ_i . By the initial assumption, \mathbf{S} is a diagonal matrix with all-different entries s_i . The eigenvectors of such a matrix are only scaled unit vectors $\mathbf{e}^{(j)}$. Thus, each \mathbf{r}_i will be a scaled unit-vector. The constraint of \mathbf{R} being an orthogonal matrix enforces the \mathbf{r}_i to be mutually different unit vectors with length 1. Therefore, \mathbf{R} necessarily has the form of a signed permutation. \square

Note that the converse is also true. If \mathbf{R} is a signed permutation matrix, $\mathbf{R}\mathbf{S}\mathbf{R}^\top$ will be diagonal.

B.3 Disjoint Mechanisms ensure identifiability

Suppose, we have identified a transformation \mathbf{H} such that $\mathbf{H}\mathbf{J}_f(g(\mathbf{z}_a))$ has disjoint rows at a certain point $\mathbf{z}_a \in \mathcal{Z}$.

(1) Since $\mathbf{M}\mathbf{f}$ is an MDE and \mathbf{g} is DMA, we can follow via Corollary 3.1 that $\mathbf{M}\mathbf{J}_f$ must have disjoint rows at every point, including $\mathbf{g}(\mathbf{z}_a)$.

(2) Now, we will show that \mathbf{H} , a matrix for which $\mathbf{H}\mathbf{J}_f(g(\mathbf{z}_a))$ also has disjoint rows, must be a permuted and scaled variant of \mathbf{M} , i.e., it must be $\mathbf{H} = \mathbf{P}\mathbf{S}\mathbf{M}$, where \mathbf{P} denotes a permutation and \mathbf{S} denotes a diagonal scaling matrix.

Since \mathbf{M} and \mathbf{H} have full rank, there exist exactly one pair of a scaling matrix \mathbf{S} and a matrix with normalized rows \mathbf{E} such that $\mathbf{H} = \mathbf{S}\mathbf{E}\mathbf{M}$.

Suppose for contradiction that \mathbf{E} was not just a permutation matrix. This means that without loss of generality, that the first row must contain at least two columns that are not equal to zero.

Since \mathbf{E} has full rank, there must be a second row with a non-zero entry in at least one of the columns. Since $\mathbf{M}\mathbf{J}_f(g(\mathbf{z}_a))$ has disjoint rows, $\mathbf{E}\mathbf{M}\mathbf{J}_f(g(\mathbf{z}_a))$ and thus $\mathbf{S}\mathbf{E}\mathbf{M}\mathbf{J}_f(g(\mathbf{z}_a)) = \mathbf{H}\mathbf{J}_f(g(\mathbf{z}_a))$ can no longer have disjoint rows. This contradicts the assumption. Hence, it must be $\mathbf{H} = \mathbf{P}'\mathbf{S}'\mathbf{M}$. Thus, $\mathbf{H}\mathbf{f} \circ \mathbf{g} = \mathbf{P}'\mathbf{S}'\mathbf{M}\mathbf{f} \circ \mathbf{g} = \mathbf{P}'\mathbf{S}'\mathbf{P}\mathbf{S} = \mathbf{P}''\mathbf{S}''$, where \mathbf{P}'' is a permutation and \mathbf{S}'' is a diagonal scaling matrix.

$\mathbf{H}\mathbf{f}$ also fulfills the min TV criterion, because it is a linear transform of the min TV encoder $\mathbf{M}\mathbf{f}$. Such a transformation cannot alter the span of the respective Jacobians (see previous proof). Thus, $\mathbf{H}\mathbf{f}$ is an MDE. \square

Note that with $\mathbf{H} = \mathbf{P}'\mathbf{S}'\mathbf{M}$, the corresponding encoder $\mathbf{H}\mathbf{f} = \mathbf{P}'\mathbf{S}'\mathbf{M}\mathbf{f}$ will be a permuted and scaled version of the an MDE. These transformation maintain disjoint rows for any $\mathbf{z} \in \mathcal{Z}$, thus $\mathbf{H}\mathbf{f}$ will fulfill the disjoint attributions criterion (Corollary 3.1).

B.4 Independent Mechanisms ensure Identifiability

First, we propose the following, extended version of Theorem 3.2.

Theorem B.1 (Identifiability under IMA). *Let \mathbf{g} adhere to IMA. Let \mathbf{f} be given with $\mathbf{f} \circ \mathbf{g} = \mathbf{D}$, where both $\mathbf{J}_f(g(\mathbf{z}))$ and $\mathbf{J}_g(\mathbf{z})$ exist $\forall \mathbf{z} \in \mathcal{Z}$. Suppose there exists an MDE $\mathbf{f}^* = \mathbf{M}\mathbf{f}$, where $\mathbf{M} \in \mathbb{R}^{K \times K}$ has full rank. Suppose we have obtained an $\mathbf{f}' = \mathbf{H}\mathbf{f}$ with a full-rank $\mathbf{H} \in \mathbb{R}^{K \times K}$.*

1. *If there is a point $\mathbf{z}_a \in \mathcal{Z}$ for which $\mathbf{J}_{f'}(g(\mathbf{z}_a))$ has orthogonal rows, then \mathbf{H} is restricted to $\mathbf{H} \in \{\mathbf{A}\mathbf{Q}\Sigma^{-\frac{1}{2}}(\mathbf{z}_a)\mathbf{M} \mid \mathbf{A} = \text{diag}(\boldsymbol{\lambda}), \boldsymbol{\lambda} \in \mathbb{R}^K > 0, \mathbf{Q}\mathbf{Q}^\top = \mathbf{I}\}$ with $\Sigma(\mathbf{z}_a)$ from Corollary 3.2, i.e., \mathbf{H} is a rotated and scaled variant of \mathbf{M} .*
2. *If there are two points $\mathbf{z}_a, \mathbf{z}_b \in \mathcal{Z}$ with orthogonal rows in $\mathbf{J}_{f'}(g(\mathbf{z}_a))$ and $\mathbf{J}_{f'}(g(\mathbf{z}_b))$ and their $\Sigma(\mathbf{z}_a)$ and $\Sigma(\mathbf{z}_b)$ differ in the sense that $\forall i, j = 1, \dots, K, i \neq j : \gamma_i \neq \gamma_j$ with $\gamma_i := \frac{\Sigma_{ii}(\mathbf{z}_b)}{\Sigma_{ii}(\mathbf{z}_a)}$, then $\mathbf{H} \in \{\mathbf{S}\mathbf{P}\mathbf{M} \mid \mathbf{S} = \text{diag}(\boldsymbol{\kappa}), \boldsymbol{\kappa} \in \mathbb{R}^K, \mathbf{P}$ a permutation matrix $\}$. I.e., \mathbf{H} must be a permuted and scaled version of \mathbf{M} and, thus, \mathbf{f}' must be an MDE.*

Proof.

(1) Before we show that \mathbf{H} is a rotated and scaled version of \mathbf{M} as given in the Theorem, let us start with constraining \mathbf{H} to a different set of solutions. Since \mathbf{M} and \mathbf{H} have full rank, there exists a non-singular matrix \mathbf{E} such that $\mathbf{H} = \mathbf{E}\mathbf{M}$. Now due to the orthogonality of \mathbf{f}' , there exists a $\boldsymbol{\kappa} \in \mathbb{R}^K$ such that $\text{diag}(\boldsymbol{\kappa}) = (\mathbf{H}\mathbf{J}_f(g(\mathbf{z}_a)))(\mathbf{H}\mathbf{J}_f(g(\mathbf{z}_a))^\top = (\mathbf{E}\mathbf{M}\mathbf{J}_f(g(\mathbf{z}_a)))(\mathbf{E}\mathbf{M}\mathbf{J}_f(g(\mathbf{z}_a))^\top = \mathbf{E}(\mathbf{M}\mathbf{J}_f(g(\mathbf{z}_a))(\mathbf{M}\mathbf{J}_f(g(\mathbf{z}_a))^\top\mathbf{E}^\top = \mathbf{E}\Sigma_a\mathbf{E}^\top$ with $\Sigma_a = \Sigma(\mathbf{z}_a)$ from Corollary 3.2. From this quadratic expression and the full rank of both matrices it follows that $\boldsymbol{\kappa} > 0$. Thus, \mathbf{E} is restricted to be from the set of solutions $\mathcal{E}_{\Sigma_a} := \{\mathbf{E} \in \mathbb{R}^{K \times K} \mid \mathbf{E}$ non-singular with $\mathbf{E}\Sigma_a\mathbf{E}^\top = \text{diag}(\boldsymbol{\kappa}), \boldsymbol{\kappa} \in \mathbb{R}^K > 0\}$.

We will now show that $\mathcal{E}_{\Sigma_a} = \Gamma := \left\{ \Lambda Q \Sigma_a^{-\frac{1}{2}} \middle| \Lambda = \text{diag}(\lambda), \lambda \in \mathbb{R}^K > 0, Q Q^\top = I \right\}$. It is easy to show that each matrix $\mathbf{F} \in \Gamma$ is indeed in \mathcal{E}_{Σ_a} , as $\mathbf{F} \Sigma_a \mathbf{F}^\top = \Lambda Q \Sigma_a^{-1/2} \Sigma_a \Sigma_a^{-1/2} Q^\top \Lambda = \text{diag}(\kappa)$ with $\kappa = \lambda^2$, and \mathbf{F} is non-singular, because $\lambda > 0$ and Q and $\Sigma_a^{-1/2}$ being non-singular.

Next, let $\mathbf{E} \in \mathcal{E}_{\Sigma_a}$. We need to find fitting λ and Q such that $\mathbf{E} = \Lambda Q \Sigma_a^{-1/2}$ to show that also every $\mathbf{E} \in \Gamma$. We know

$$\mathbf{I} = \mathbf{K}^{-1/2} \mathbf{E} \Sigma_a \mathbf{E}^\top \mathbf{K}^{-1/2} = \underbrace{(\mathbf{K}^{-1/2} \mathbf{E} \Sigma_a^{1/2})}_{Q} \underbrace{(\Sigma_a^{1/2} \mathbf{E}^\top \mathbf{K}^{-1/2})}_{Q^\top}$$

where $\mathbf{K} := \text{diag}(\kappa)$, which gives us a candidate for Q . By now choosing $\lambda = \sqrt{\kappa}$ (and thus $\Lambda = \mathbf{K}^{-1/2}$), which is well-defined since $\kappa > 0$, we have that $\Lambda Q \Sigma_a^{-1/2} = \mathbf{E}$, i.e., $\mathbf{E} \in \Gamma$.

In summary, we have shown that $\mathbf{H} = \Lambda Q \Sigma_a^{*-1/2} \mathbf{M}$, where Λ can be any positive scaling matrix and Q is any rotation matrix.

(2) Our goal is now, under the additional condition on \mathbf{z}_a and \mathbf{z}_b , to constrain the form of \mathbf{H} further than in (1). First, by using (1) on \mathbf{z}_a , we have that $\mathbf{H} = \Lambda Q \Sigma_a^{-1/2}$. Now, since $\mathbf{J}_{f'}$ is also orthogonal at \mathbf{z}_b , there exists some $\mu \in \mathbb{R}_{\neq 0}^K$ such that

$$\text{diag}(\mu) = (\mathbf{H} \mathbf{J}_f(g(\mathbf{z}_b))) (\mathbf{H} \mathbf{J}_f(g(\mathbf{z}_b)))^\top \quad (5)$$

$$= (\Lambda Q \Sigma_a^{-1/2} \mathbf{M} \mathbf{J}_f(g(\mathbf{z}_b))) (\Lambda Q \Sigma_a^{-1/2} \mathbf{M} \mathbf{J}_f(g(\mathbf{z}_b)))^\top \quad (6)$$

$$= \Lambda Q \Sigma_a^{-1/2} \Sigma_b \Sigma_a^{-1/2} Q^\top \Lambda \quad (7)$$

with $\Sigma_b = \Sigma(\mathbf{z}_b)$. With the NEMR conditions of the theorem on γ_i , $\Sigma = \Sigma_a^{-1/2} \Sigma_b \Sigma_a^{-1/2}$ is a diagonal matrix with entries γ_i that are all different. Thus,

$$\text{diag}(\mu) = \Lambda Q \text{diag}(\gamma) Q^\top \Lambda \quad (8)$$

$$\iff \text{diag}(\mu \lambda^{-2}) = Q \text{diag}(\gamma) Q \quad (9)$$

Lemma B.1 states that, with all entries of γ being different, Q can only be a signed permutation matrix \mathbf{P} . Thus, $\mathbf{H} = \Lambda \mathbf{P} \Sigma_a^{-1/2} \mathbf{M}$. We can further move the signs of the permutation into Λ' , such that $\mathbf{H} = \Lambda' \mathbf{P}' \Sigma_a^{-1/2} \mathbf{M}$. Because $\mathbf{P}' \Sigma_a^{-1/2} = (\mathbf{P}' \Sigma_a^{-1/2} \mathbf{P}'^\top) \mathbf{P}'$ and according to the converse of Lemma B.1, $\mathbf{P}' \Sigma_a^{-1/2} \mathbf{P}'^\top$ will be diagonal, we can express $\mathbf{H} = \Lambda'' \mathbf{P}' \mathbf{M}$, i.e., H is a scaled permuted variant of \mathbf{M} .

This makes $f' = \mathbf{H} f = \Lambda'' \mathbf{P}' \mathbf{M} f = \Lambda'' \mathbf{P}' f^*$ an MDE, as it fulfills the first requirement by definition and also has min TV (analogous argumentation to previous proof). Also note that this implies that $\mathbf{J}_{f'}$ is not only orthogonal at \mathbf{z}_a and \mathbf{z}_b , but at all points \mathbf{z} , because all MDEs of IMA processes fulfill orthogonal attributions (Corollary 3.2). \square

In the next section, we discuss how the proofs can be turned into analytical solutions to find MDEs.

B.5 Analytical Solutions to Minimal Disentangled Encoders

B.5.1 Disjoint Mechanisms

Under perfect DMA conditions of the entangled encoder and linearly distorted MDEs, we can compute an analytical solution for \mathbf{H} , that will result in a DMA encoder. Suppose we are provided with a gradient matrix $\mathbf{J}_f(\mathbf{x}_a) \in \mathbb{R}^{K \times L} = \mathbf{M}^{-1} \mathbf{J}_{f^*}(\mathbf{x}_a)$, where \mathbf{J}_{f^*} is an MDE, such that its Jacobian has disjoint rows. We propose the following steps:

1. Find a submatrix $\mathbf{J}_{reg} \in \mathbb{R}^{K \times K}$ of K linearly independent columns in $\mathbf{J}_f(\mathbf{x}_a)$, such that $\det(\mathbf{J}_{reg}) \neq 0$.
2. Compute and return $\mathbf{H} = \mathbf{J}_{reg}^{-1}$

The first step ensures that gradients for precisely one pixel affected by each component are selected. This can be seen as follows: Because we suppose \mathbf{M} has full rank and \mathbf{J}_{reg} can be written as $\mathbf{J}_{reg} = \mathbf{M}^{-1} \mathbf{J}_{f^*,reg}$, where $\mathbf{J}_{f^*,reg}$ is a square submatrix with selected columns of \mathbf{J}_{f^*} , the submatrix $\mathbf{J}_{f^*,reg}$ also needs to be of full rank. Because of the DMA principle, $\mathbf{J}_{f^*,reg}$ again needs to be of the form $\mathbf{P} \mathbf{S}$ with one component active in each column. Furthermore, $\mathbf{H} = \mathbf{J}_{reg}^{-1} = (\mathbf{M}^{-1} \mathbf{P} \mathbf{S})^{-1} = \mathbf{S}^{-1} \mathbf{P}^{-1} \mathbf{M}$. As the inverses of scaling and permutation matrices have the same respective form again, \mathbf{H} is a scaled and permuted version of \mathbf{M} .

Algorithm 1: DA concept discovery with SGD.

Input: encoder f , images $\{\mathbf{x}_n\}_{n=1,\dots,N}$
 $Jacobians \leftarrow \text{Gradient}(f, \{\mathbf{x}_n\}_{n=1,\dots,N}).detach()$
 $H \leftarrow K\text{-dim identity matrix}$
for L epochs, $J_f(\mathbf{x}) \in Jacobians$ **do**
 $U \leftarrow |\mathbf{H}J_f(\mathbf{x})|$ // No absolute value operation here for DA
 $U \leftarrow \text{row-normalize } U$
 $\text{loss} \leftarrow \|\mathbf{U}\mathbf{U}^\top - \mathbf{I}_K\|_F$
 $\text{loss.backwards}()$
end
return H

Algorithm 2: Concept discovery via Clustering of analytical solutions.

Input: encoder f , images $\{\mathbf{x}_n\}_{n=1,\dots,N}$, DA/OA flag
 $Jacobians \leftarrow \text{Gradient}(f, \{\mathbf{x}_n\}_{n=1,\dots,N}).detach()$
for $i \in 1 \dots N$, $J_f(\mathbf{x}_i) \in Jacobians$ **do**
 if DA **then**
 | $H_i \leftarrow \text{computeAnalyticalDA}(J_f(\mathbf{x}_i))$
 if OA **then**
 | $H_i \leftarrow \text{computeAnalyticalOA}(J_f(\mathbf{x}_i), J_f(\mathbf{x}_{i+1}))$ // OA needs two Jacobians for H
 | $H_i \leftarrow \text{row-normalize } H_i$
end
 $C \in \mathbb{R}^{2K \times K} \leftarrow \text{sphericalCluster}(\{H_i[j, :] \mid i \in 1 \dots N, j \in 1, \dots, K\}, \text{n_clusters} = 2K)$ // cluster rows in the H_i , return 2K cluster centers in rows of C
 $H \in \mathbb{R}^{K \times K} \leftarrow \text{mergePoles}(C)$ // merge rows of opposite signs
return H

B.5.2 Independent Mechanisms

Suppose we are given matrices $\Gamma_a = J_f(\mathbf{x}_a)J_f(\mathbf{x}_a)^\top = \mathbf{M}^{-1}\Sigma_a\mathbf{M}^{-\top}$ and $\Gamma_b = J_f(\mathbf{x}_b)J_f(\mathbf{x}_b)^\top$. We then apply the following steps

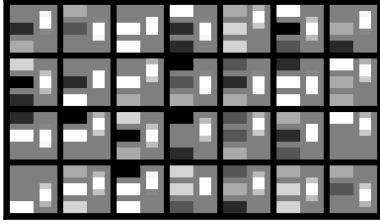
1. $\mathbf{U} = \text{inverse}((\text{cholesky}(\Gamma_a)))$
2. $\mathbf{V} = \text{eigenvectors}(\mathbf{U}\Gamma_b\mathbf{U}^\top)$
3. **return** $\mathbf{H} = \mathbf{V}^\top\mathbf{U}$

The first step implies that $\mathbf{U}^{-1}\mathbf{U}^{-\top} = \Gamma_a$ and that $\mathbf{U}\Gamma_a\mathbf{U}^\top = \mathbf{I}$. We have thus identified the matrix \mathbf{E} from the first theorem, which has the form $\mathbf{U} = \Lambda^{1/2}\mathbf{Q}\Sigma_a^{-1/2}\mathbf{M}$. In step two we compute $\mathbf{U}\Gamma_b\mathbf{U}^\top = \Lambda^{1/2}\mathbf{Q}\Sigma_a^{-1/2}\Sigma_b\Sigma_a^{-1/2}\mathbf{Q}^\top\Lambda^{1/2} = \mathbf{R}\mathbf{V}^\top$, where \mathbf{R} hold the eigenvalues. Accordingly, by left and right multiplying with \mathbf{V} , we observe that $(\mathbf{V}^\top\mathbf{U})\Gamma_b(\mathbf{V}^\top\mathbf{U})^\top = \mathbf{R}$, i.e., $(\mathbf{V}^\top\mathbf{U})$ solves the orthogonality problem for Γ_b . We can easily verify that $\mathbf{H} = \mathbf{V}^\top\mathbf{U}$ is also a solution for Γ_a by computing $\mathbf{V}^\top\mathbf{U}\Gamma_a\mathbf{U}^\top\mathbf{V} = \mathbf{I}$. By the identifiability result, $\mathbf{H} = \mathbf{V}^\top\mathbf{U} = \Lambda\mathbf{P}\mathbf{M}$, a scaled and permuted version of \mathbf{M} , if the additional gradient ratio condition is fulfilled with \mathbf{x}_a and \mathbf{x}_b .

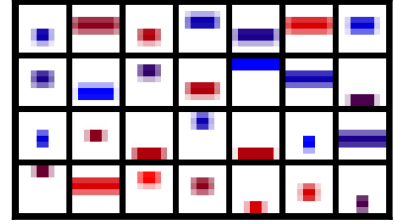
B.6 Algorithms

We present the SGD optimization for DA in Algorithm 1. Note that the algorithm for OA optimization via SGD can be obtained by just omitting the absolute value operation in the line indicated by the comment.

We further derive a clustering strategy that allows aggregating many analytical solutions, that are subject to noise. It is provided in Algorithm 2 and directly based on our identifiability theorems. They state that a scaled and permuted version of the distortion \mathbf{M} will be identified. We can compute a batch of analytical solution for data samples (one Jacobian required for DA, two for OA). However, when facing noise, there is a need to aggregate and average different solutions, which can only be done if the same scaling and permutations are used. The scaling can be undone easily by applying a row-wise normalization. However, we still face permutations and possibly opposite signs in the remaining



(a) Random samples in the FourBars dataset.



(b) Random samples in the ColorBar dataset.

Figure 6: Random samples drawn from the synthetic datasets.

rows of the matrices. Therefore, we apply an implementation of the K-Means algorithm on a unit sphere.³ By this approach we identify $2K$ cluster centers, corresponding to the directions with either positive or negative signs. We merge the directions with opposite signs by a greedy strategy: We always pick the most diametrical pair of vectors (lowest cos-distance) to be merged and only return one of them as a row in the final matrix \mathbf{H} . The two merged direction are removed from the list of cluster centers and the next directions to be merged will be selected until only K directions are in the rows of the final matrix \mathbf{H} that is returned.

B.7 Extending gradients to general attributions

We make an initial attempt to generalize our method, considering gradients as a simple form of attribution method. Intuitively, $\mathbf{J}_f = \nabla_{\mathbf{x}}(f(\mathbf{x}))$ contains input gradients (termed grad in the remainder) which can be thought of as a simple form of attribution for each component [39, 38]. Thus, on a more general level, our proposed approach optimizes for the disjointness of attributions. Thus, we may use other forms of *homogeneous attributions* in place of \mathbf{J}_f . These are local attribution methods $A_f : \mathbb{R}^L \rightarrow \mathbb{R}^{K \times L}$ for the encoder f with $A_{Hf}(\mathbf{x}) = \mathbf{H}A_f(\mathbf{x})$ that map an instance \mathbf{x} to a matrix of attributions for each latent dimension. Besides the above input gradients, this class contains other popular methods such as integrated gradients (IG) [41] and smoothed gradients (SG) [40] (because these methods are linear in f). Thus, we can formulate a generalized *disjoint attributions objective*:

$$\min_{\mathbf{H}} \sum_{n=1}^N \left\| \left| \overline{HA_f(\mathbf{x})} \right| \left| \overline{HA_f(\mathbf{x})} \right|^{\top} - I_K \right\|_F^2. \quad (10)$$

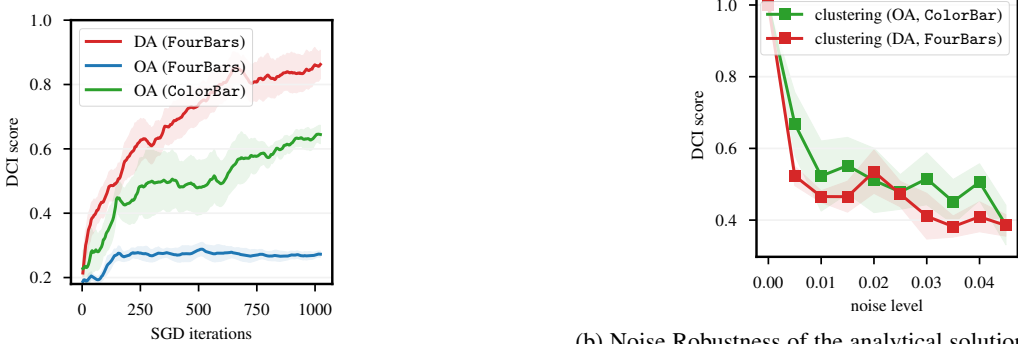
C Experimental Details

C.1 Synthetic datasets

We show random samples from both datasets in Figure 6. We provide two additional graphics with the results on the synthetic datasets in Figure 7. They show that SGD exhibits a convergence behaviour as predicted by our theory and comparable to the analytical solutions. Furthermore, the results indicate that the analytical solutions is not very robust to noise.

C.2 Architectures

For the disentanglement models, we use the implementations provided by the open source library `disentanglement-pytorch`⁴. For the evaluation measures, we use the implementation of `disentanglement_lib`⁵ with their respective default parameters. We use a simple encoder and decoder architecture, that consists of five and six feed-forward convolutional layers respectively and relies on the ReLU activation function.



(a) Disentangling gradients of synthetic datasets with SGD. On the **FourBars** dataset, OA fails to iterate towards a disentangled solution, because the non-equal magnitudes condition is violated. However, OA converges on the **ColorBar** dataset, although at a slower rate.

(b) Noise Robustness of the analytical solution. We investigate the robustness of the semi-analytical clustering approaches to noisy gradients and find that they react highly sensitive, making them unsuitable for practical applications.

Figure 7: Additional results on the synthetic datasets.

C.3 Correlated sampling

In this paper, we use two methods to introduce correlations between the ground truth components. Both methods rely on proportional resampling: We first draw a batch that has multiple times the final batch size (we use factors from 3-6 depending on the non-uniformity of the distribution), then compute the (unnormalized) probability of each sample under a given distribution over the component values, and then resample a final batch (with replacement) proportional to these probabilities.

The two methods differ in the probability distribution assigned to the component values. The first setting (used in Sec. 4.2) uses the approach of Träuble et al. [43]: As visualized in Fig. 8(a) to (c), we pick two components z_1 and z_2 , create the grid of possible values, and then lay a diagonal line over this grid. Along this line, we set a normal distribution with a standard deviation s . A higher s means that the distribution gives a higher probability to more component combinations of the grid, whereas a smaller s is more restrictive. Mathematically, it is defined by Träuble et al. [43] as:

$$p(z_1, z_2) \propto \exp\left(-\frac{(z_1 - \alpha z_2)^2}{2s^2}\right), \quad (11)$$

where $\alpha = z_1^{\max}/z_2^{\max}$ brings the components to a same scale and s is similarly normalized to the maximum values that z_1 and z_2 can take. The remaining components $z_i, i > 2$, are marginalized out of this distribution and thus continue to be sampled uniformly at random.

This setting is limited to one pair of components and also introduces a non-Gaussian distribution over all components. To tackle these limitations and thus to make the distributional challenge harder, we use a different probability distribution in Sec. 4.3. Here, we lay a normal distribution over *all* components, i.e., $z \sim \mathcal{N}(\mu, \Sigma)$, where μ is centered in the middle of the possible values, i.e., $\mu = \frac{z^{\max} - z^{\min}}{2}$. Σ is similarly normalized, since we decompose it into $\Sigma = \text{diag}(\sigma^2)\Gamma$.

The vector $\sigma \in \mathbb{R}_{>0}^K$ gives standard deviations for each component via $\sigma^2 = \left(\frac{\mu+0.5}{2}\right)^2$ such that the distribution stretches across the grid of possible values. Note that the $+0.5$ is because the values are assumed to be zero-indexed. Γ is a correlation matrix with 1 on its diagonal. In the first experiment in Sec. 4.3, we correlate only one pair of variables and set their corresponding off-diagonal entries in Γ to ρ . Fig. 8 (d) to (f) show the corresponding marginal distributions of these components. In the second experiment, we fill Γ with several correlations in the following order:

$$\begin{matrix} z_1 \\ z_2 \\ z_3 \\ z_4 \\ z_5 \\ z_6 \end{matrix} \left(\begin{array}{cccccc} 1 & 4 & 12 & 14 & 9 & \\ & 11 & 5 & 10 & 6 & \\ & & 3 & 8 & 15 & \\ & & & 13 & 7 & \\ & & & & 2 & \\ & & & & & \end{array} \right) \quad (12)$$

³We use the implementation from <https://github.com/jasonlaska/spherecluster>

⁴<https://github.com/amir-abdi/disentanglement-pytorch>

⁵https://github.com/google-research/disentanglement_lib

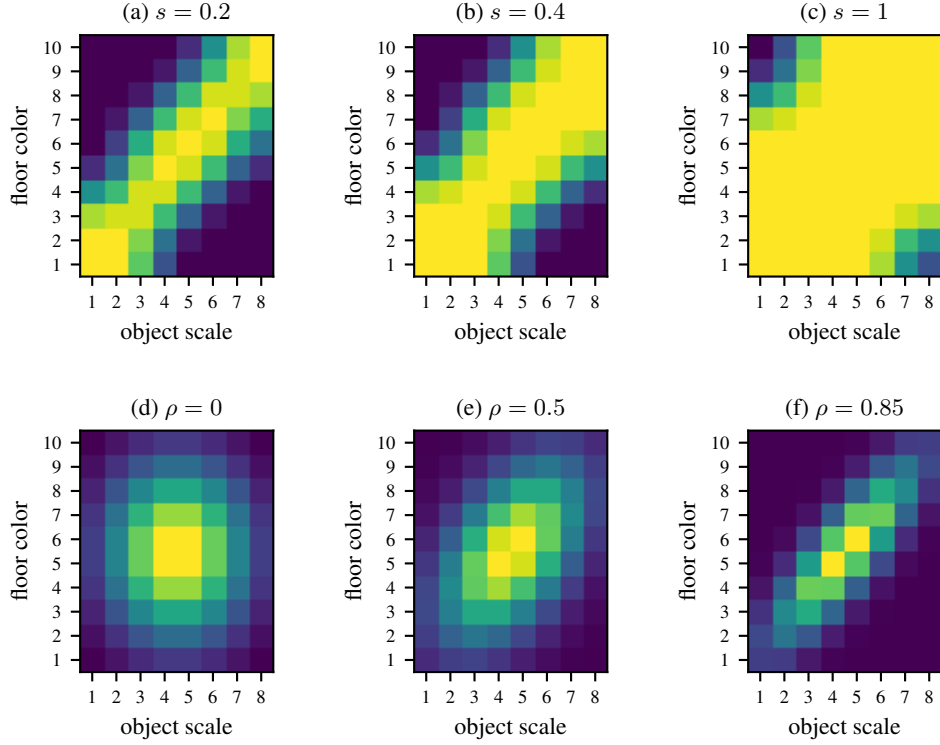


Figure 8: Exemplary correlated densities of the components floor color and object scale under the correlated sampling setup of Greselle et al. [15] (a – c) and with our Gaussian sampling (d – f). The correlation strength is indicated on top. Purple denotes a low and yellow a high density.

where the component order of the rows and columns is $z_1 = \text{floor_color}$, $z_2 = \text{background_color}$, $z_3 = \text{object_color}$, $z_4 = \text{object_scale}$, $z_5 = \text{object_shape}$, $z_6 = \text{orientation}$. Here, it is important to ascertain that the covariance matrix stays positive definite. Thus, we start with $\rho = 0.7$, check if the lowest eigenvalue of Σ is at least 0.2, and if not, reduce ρ by a factor of 0.9 until the eigenvalue fulfills this property. While technically it would be enough to have the smallest eigenvalue anywhere above 0, we found that 0.2 helps in numerical stability, for instance when inverting the covariance matrix to compute the multivariate normal distribution density.

C.4 Discriminative setup

The decision tree that is used to generate the class distribution is shown in Figure 9. It relies on 4 (binarized) components. We trained a simple CNN classifier for this problem using the cross-entropy loss. In addition to the classification loss terms, we add a regularizer $\|z\|_2^2$, which constrains the latent codes to not grow arbitrarily large, during training. To create a realistic setup, we subsample the dataset to follow a normal distribution as shown in Fig. 8d. We also add label noise near the decision boundary: For objects which have an orientation that is nearly centered, we follow each branch (left/right) with a probability of 50 %. With increasing left-orientedness, the probability of following the left branch increases to almost 100 % in form of a sigmoid function over the actual orientation. We follow the same procedure for the remaining features. We train the classifier for 10k iterations at a batch size of 24 and verify that it reaches an accuracy close to the best-possible one taking the mislabeled samples into account. We add correlations by increasing the chance of the the factors *obj. color* and *floor color* taking the same binary value. We use our disjoint attributions approach to find a $H \in \mathbb{R}^{4 \times 6}$ matrix that should map the 6-dimensional latent space of the model to the four binary concepts that are used in the classification task. For the unit directions, we take the first four unit directions of the latent space, for PCA and ICA, we take the most prominent for components discovered for the evaluation with the four annotated ground truth concepts.

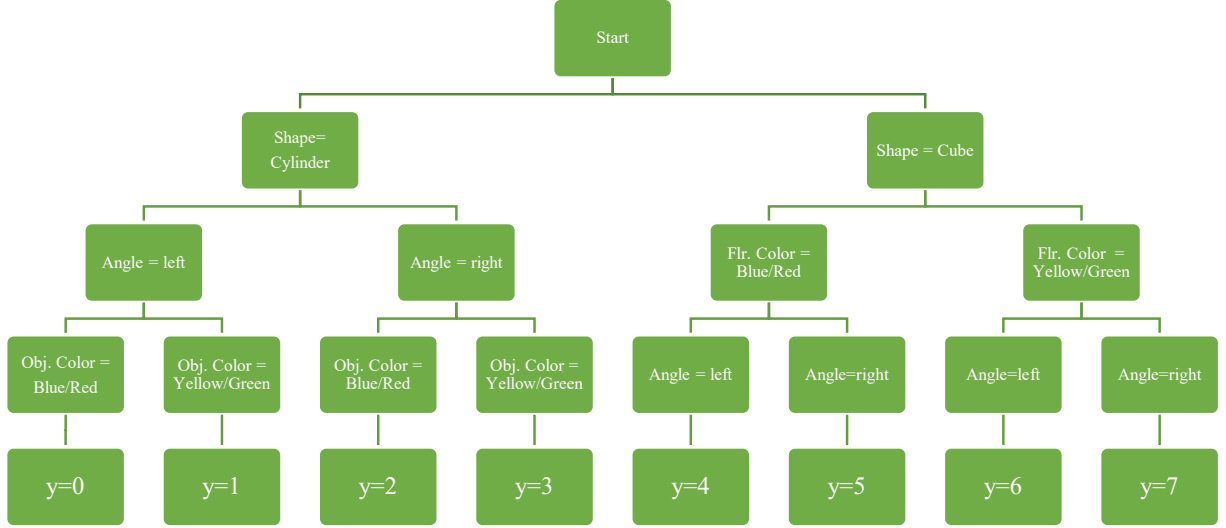


Figure 9: The decision tree setup that we use for the discriminative classification problem. Each image is assigned one out of eight class labels y according to the following decision tree.

C.5 Evaluation scores

Several scores to quantify disentanglement have been proposed in the literature and often emphasize a different aspect of disentanglement [37]. Among the most common scores is the Disentanglement-Completeness-Informativeness score (DCI) by Eastwood and Williams [11]. In their work, they propose a metric to measure Disentanglement, that relies on training predictors $\hat{z}_j = f_j(e)$ to predict each individual ground truth component z_j from the learned latent representation e . Furthermore, they compute normalized importance weights P_{ik} that quantify how important learned component e_i is for predicting the ground component z_k . The disentanglement metric computes a row-wise entropy over the P -matrix, which assigns a score of 1, if the learned component e_i is useful for predicting only a single factor and as score of 0, if it is equally useful for predicting all factors. Other commonly used metrics include the Mutual Information Gap (MIG) [9], Separated Attribute Predictability (SAP) [28] and the FactorVAE metric [25]. However, it is unclear which of these metrics (or if any) also provide useful results in the correlated setting Träuble et al. [43]. Therefore, to compute the reliable evaluations, we train the model (and the post-processing methods such as PCA, ICA, OA, DA) on the correlated dataset, but compute the metrics on samples from the full, *uncorrelated* datasets to avoid distortion in our scores. Träuble et al. noted that the DCI scores were able to discover entanglement between 2 variables [43, Figure 11, Appendix], whereas most other metrics failed even in this case. Therefore, we mainly rely on this score for our experiments but also report results for the other scores in Experiment Sec. 4.2 that show a similar picture in this appendix (Appendix D.4).

C.6 CUB experiments

CUB-200-2011 is a fine-grained dataset containing a total of 11,788 images of 200 bird species (5994 for training and 5794 for testing). We trained a ResNet-50 with two fully-connected (fc) layers (the second fc layer served as a bottleneck layer and took 2048-dim feature vectors as input and output 512-dim ones) on CUB for 100 epochs using a SGD optimizer with an initial learning rate of 0.001. The input images were center cropped to 224×224 pixels. Trained on a standard cross-entropy loss, the ResNet achieved a classification accuracy of on average 77.47% on five random seeds, indicating proper training. After training the classifier, we applied our proposed method to discover components in the embedding space.

CUB provides no ground-truth components since it is a real-world dataset. It does, however, contain 312 attributes semantically describing the bird classes, e.g., wing color or beak shape. These attributes have no guarantee to be complete, but they offer 312 interpretable components. This allows for an attempt to quantify whether our discovered components are interpretable and meaningful by comparing whether they match some of these interpretable ones.

Formally, we are given a set of image feature embeddings $\{e_n\}_{n=1,\dots,N}$, $e_n \in \mathbb{R}^L$ and a found matrix $H = (h_1, \dots, h_K) \in \mathbb{R}^{L \times K}$ that contains the directions of discovered components ($L = 512$, $K = 30$). A score s_n^k of

Model	Ranges
BetaVAE	$\beta \in \{1, 2, 4, 6, 8, 16\}$
FactorVAE	$\gamma \in \{5, 8, 10, 20, 30, 40, 50, 100\}$
BetaTCVAE	$\beta \in \{1, 2, 4, 6, 8, 10\}$
DIPVAE	$\lambda_{od} \in \{1, 2, 5, 10, 20, 50\}$

Table 3: The hyperparameter ranges considered in this work.

n -th image for the k -th discovered component can be calculated by projecting the feature embeddings on that component direction, i.e., $s_n^k = \langle e_n, h_k \rangle$. One pitfall is that s_n^k can be negative, indicating, e.g., a non-black bird for the component "primary color: black", but this opposite attribute is usually encoded in a separate attribute in CUB, e.g., "primary color: white". Thus, we separate the negative and positive values into two components (where we set values of the opposite sign to 0), resulting in $2 \cdot K$ positive scores for each image.

To compare these component scores with the attributes, we make use of the numerical attribute values provided in CUB. First, we average the $2 \cdot K$ component values of all images of a class, to be comparable with the class-wise attributes provided by CUB. This gives us a numerical $2 \cdot K$ dimensional component description and a 312 dimensional attribute description per class. Now, we match the discovered components to the attributes. We compare each discovered component to each attributes via the Spearman's rank correlation coefficient and consider the attribute with the highest score to match the component. These are the matches used in Sec. 4.5. We further use the (average) Spearman's rank correlation across all components to their best-matching attributes to quantify how well the components match to interpretable attributes in Appendix D.6.

C.7 Hyperparameters for the disentanglement models

We orient our hyperparameter ranges by the works of Träuble et al. [43], Locatello et al. [30]. The exact ranges are provided in Tab. 3. We find the best hyperparameters in the ranges for each correlation strength/dataset/model triple separately. Then we train five models from independent seeds to run our experiments. We use the Adam optimizer for all model with a learning rate of 10^{-4} , batch size of 64 and train for 300k iterations (equiv. to 40 epochs on Shapes3D).

For the optimization of the post-hoc disentanglement problem, we use slightly different hyperparameters. We use the RMSProp optimizer with learning rate of 10^{-3} and a batch size of 48.

D Additional results

D.1 Reconstruction quality

As a check, we investigate the reconstruction quality of the disantangle models. For the 3D shapes, the reconstruction is very high, but we observe some more serious reconstruction errors on the MPI-3d dataset: (Appendix D.2). Figures 10 and 11 show the original images on the left and the reconstructions of a randomly chosen BetaVAE on the right. On Shapes3D, the BetaVAE is able to reconstruct the image from its embedding representation. On MPI3D-real, it is able to reconstruct the big image parts shared across many pictures (ground, background stripe and background), but becomes blurry in the smaller and more nuanced robot arm and object shapes. This indicates that the information on these components might not be stored in the embedding space and is thus hardly disentangable. A longer training (800k instead of 300k iterations) did not resolve the issue. The issue might arise, following Gondal et al. [13], because the input images were scaled down to 64x64 pixels making the detailed objects hard to perceive, and because the same architecture as in the Shapes3D experiments was used, which might not be expressive enough.

Dataset	MPI3D-real			
	Correlated components	background & object color	background & robot arm dof-1	robot arm dof-1 & robot arm dof-2
BetaVAE	0.340 \pm 0.027	0.277 \pm 0.026	0.300 \pm 0.046	
	+PCA	0.116 \pm 0.008	0.174 \pm 0.021	0.154 \pm 0.015
	+ICA	0.237 \pm 0.042	0.205 \pm 0.023	0.180 \pm 0.021
	+Ours (OA)	0.355 \pm 0.033	0.349 \pm 0.015	0.337 \pm 0.038
	+Ours (DA)	0.334 \pm 0.025	0.317 \pm 0.028	0.278 \pm 0.030
FactorVAE	0.205 \pm 0.022	0.239 \pm 0.017	0.171 \pm 0.005	
	+PCA	0.179 \pm 0.010	0.234 \pm 0.012	0.171 \pm 0.006
	+ICA	0.066 \pm 0.009	0.090 \pm 0.006	0.073 \pm 0.011
	+Ours (OA)	0.201 \pm 0.019	0.226 \pm 0.010	0.191 \pm 0.011
	+Ours (DA)	0.184 \pm 0.013	0.218 \pm 0.016	0.180 \pm 0.013
BetaTCVAE	0.383 \pm 0.022	0.359 \pm 0.026	0.309 \pm 0.036	
	+PCA	0.356 \pm 0.022	0.328 \pm 0.017	0.295 \pm 0.038
	+ICA	0.245 \pm 0.041	0.260 \pm 0.024	0.170 \pm 0.045
	+Ours (OA)	0.323 \pm 0.025	0.316 \pm 0.029	0.271 \pm 0.033
	+Ours (DA)	0.327 \pm 0.027	0.325 \pm 0.025	0.272 \pm 0.033
DipVAE	0.235 \pm 0.019	0.181 \pm 0.049	0.232 \pm 0.040	
	+PCA	0.090 \pm 0.005	0.088 \pm 0.028	0.091 \pm 0.011
	+ICA	0.234 \pm 0.019	0.180 \pm 0.048	0.232 \pm 0.041
	+Ours (OA)	0.230 \pm 0.022	0.182 \pm 0.048	0.230 \pm 0.042
	Ours (DA)	0.249 \pm 0.026	0.188 \pm 0.049	0.253 \pm 0.051

Table 4: Mean \pm std. err. of the DCI scores (across all components of the dataset) of several models and post-hoc methods applied to their embeddings. Columns show which pair of components was correlated during training.

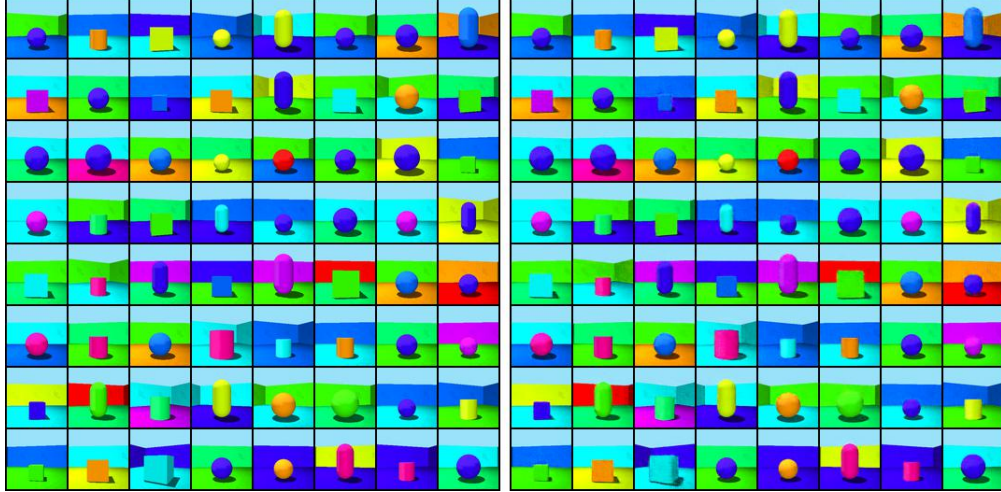


Figure 10: Random example images (left) and their reconstructions (right) of a BetaVAE on Shapes3D.

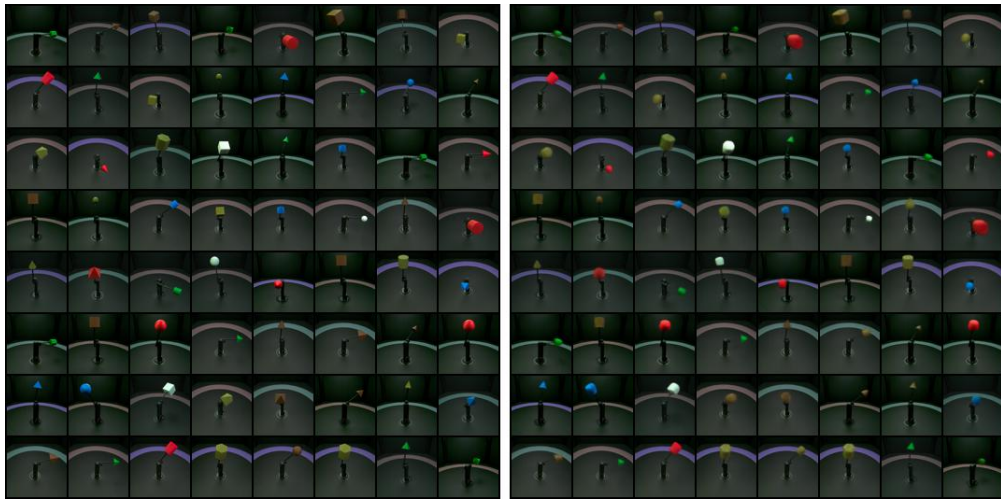


Figure 11: Random example images (left) and their reconstructions (right) of a BetaVAE on MPI3D-real.

D.2 Results for the MPI-3D dataset

In addition to 3Dshapes, we use the challenging MPI3D-real dataset [13], which consists of realistic images of a moving robot arm. It is by far more challenging, as the component is only present in a small portion of the images, and the data consists of real photographs. We report the results on this dataset in Table 4. We saw low disentanglement scores of both the base and post-hoc models on MPI3D-real compared to the performance on Shapes3D. This implies that the embedding spaces of the VAEs was not trained well. In fact, this is supported by the reconstruction quality considerations on both Shapes3D and MPI3D-real. Because our approaches are based on the given embeddings, they also struggle when they incorrectly reflect the sample.

D.3 Correlation strengths and attribution methods in first experiment

In this section we provide additional ablations for the rectification experiment in Sec. 4.2. We investigate the impact of the choice of attribution method and the correlation strength s . The values (DCI scores) are shown in Tab. 7. As expected, our approach offers the highest gains over the baseline when the correlation is higher. Starting at $s = 0.4$, our runs start to reliably outperform the baselines. Regarding the attributions, there is no clear picture, but Grad and SG seem to yield good results more stably across runs. DA usually outperforms OA, which supports our theoretical results on identifiability.

Dataset	Shapes3D		
	floor vs. background	orientation vs. background	orientation vs. size
BetaVAE	0.497 ± 0.028	0.581 ± 0.044	0.491 ± 0.049
+PCA	0.263 ± 0.028	0.310 ± 0.025	0.324 ± 0.041
+ICA	0.574 ± 0.040	0.540 ± 0.080	0.577 ± 0.038
+OA-SGD	0.617 ± 0.018	0.602 ± 0.050	0.579 ± 0.032
+OA-Clust	0.510 ± 0.255	0.473 ± 0.236	0.545 ± 0.273
+DA-SGD	0.641 ± 0.031	0.624 ± 0.055	0.627 ± 0.031
FactorVAE	0.507 ± 0.105	0.502 ± 0.076	0.712 ± 0.010
+PCA	0.358 ± 0.075	0.474 ± 0.051	0.556 ± 0.029
+ICA	0.294 ± 0.070	0.263 ± 0.053	0.340 ± 0.034
+OA-SGD	0.551 ± 0.040	0.498 ± 0.034	0.595 ± 0.051
+OA-Clust	0.248 ± 0.124	0.352 ± 0.176	0.235 ± 0.117
+DA-SGD	0.584 ± 0.047	0.510 ± 0.055	0.556 ± 0.038
BetaTCVAE	0.619 ± 0.008	0.613 ± 0.041	0.659 ± 0.005
+PCA	0.400 ± 0.030	0.421 ± 0.068	0.450 ± 0.065
+ICA	0.540 ± 0.023	0.497 ± 0.036	0.627 ± 0.023
+OA-SGD	0.623 ± 0.021	0.652 ± 0.028	0.638 ± 0.037
+OA-Clust	0.647 ± 0.323	0.633 ± 0.316	0.659 ± 0.330
+DA-SGD	0.666 ± 0.010	0.664 ± 0.023	0.748 ± 0.026
DipVAE	0.631 ± 0.018	0.652 ± 0.017	0.548 ± 0.036
+PCA	0.158 ± 0.013	0.160 ± 0.020	0.170 ± 0.022
+ICA	0.630 ± 0.018	0.651 ± 0.017	0.542 ± 0.033
+OA-SGD	0.644 ± 0.019	0.624 ± 0.014	0.558 ± 0.051
+OA-Clust	0.639 ± 0.319	0.613 ± 0.306	0.521 ± 0.260
+DA-SGD	0.684 ± 0.009	0.679 ± 0.013	0.601 ± 0.055

Table 5: Mean \pm std. err. of the DCI scores of four post-hoc methods applied to the embedding spaces of four disentanglement models on two datasets with different pairs of correlated variables. We compare our OA and DA methods to the clustering strategy that relies on analytical solutions.

Dataset	Shapes3D
Correlated factors	floor vs. background
BetaVAE	0.579 ± 0.089
+PCA	0.291 ± 0.033
+ICA	0.435 ± 0.076
+OA-SGD	0.738 ± 0.072
+DA-SGD	0.868 ± 0.025
FactorVAE	0.684 ± 0.163
+PCA	0.526 ± 0.136
+ICA	0.363 ± 0.097
+OA-SGD	0.779 ± 0.063
+DA-SGD	0.847 ± 0.072
BetaTCVAE	0.589 ± 0.005
+PCA	0.388 ± 0.046
+ICA	0.609 ± 0.065
+OA-SGD	0.876 ± 0.027
+DA-SGD	0.754 ± 0.127
DipVAE	0.615 ± 0.114
+PCA	0.429 ± 0.169
+ICA	0.585 ± 0.024
+OA-SGD	0.798 ± 0.099
+DA-SGD	0.782 ± 0.009

Table 6: Mean \pm std. err. of the DCI scores of four post-hoc methods applied to the embedding spaces of four disentanglement models on two datasets with different pairs of correlated variables. The DCI is computed across **the two correlated components** of the dataset.

D.4 Further disentanglement metrics and algorithm

Tables 8 – 10 show the results of the experiment in Sec. 4.2 measured in the alternative metrics MIG, FactorVAE and SAP score. For MIG, we see similar results as for DCI in Section 4.2 and in Table 4. The results in FactorVAE and SAP score are slightly inferior but our approach still improves over the baseline in many setups.

We add the clustering approach given in Algorithm 2 to the set of competitors. The results are given in Table 5. While it is able to beat the baselines for 8/12 setups, it does not reach the level of the DA method with SGD optimization. We also compute the disentanglement only on the two correlated components for the first pair of factors in Table 6. This emphasized the improvement introduced by our OA and DA approaches.

D.5 Qualitative results on Shapes3D

In this section, we want to show another traversal plot like the one in Fig. 1 and more thoroughly analyze its latent space. We chose another architecture (BetaTCVAE) and $s = 0.2$ with the usual correlated factors *floor color* and *background color*. Out of the 5 independent runs, we selected the one with the highest DCI score (of the base model) for the analysis.

Linear entanglement matrix. To study which factors are encoded in which latent dimension, we compute a matrix of linear entanglement. By our linear entanglement hypothesis, $\mathbf{z}' = \mathbf{D}\mathbf{z}$, where the matrix $\mathbf{D} = [\mathbf{d}_1, \dots, \mathbf{d}_K] \in \mathbb{R}^{K \times K}$ contains the directions $\mathbf{d}_i \in \mathbb{R}^K$, in which the ground truth concepts are encoded. Changing the component i (entry z_i) by one unit will change the resulting embedding by \mathbf{d}_i . To find these \mathbf{d}_i , we take the factors at the origin of the traversal plot and alter only a single component i . We then encode the image corresponding to that change, and measure the change in embeddings to find the linear direction \mathbf{d}_i that the corresponding component is encoded in (to be precise, we sample several changes and take the largest eigenvector of the embedding changes covariance). Thus, we can estimate the matrix \mathbf{D} . An example is shown in Fig. 12a and provides evidence that linear entanglement is possible when training autoencoder models from correlated data.

Model Correlation	BetaVAE			FactorVAE			BetaTCVAE			DIPVAE		
	$s = 0.2$	$s = 0.4$	$s = \infty$	$s = 0.2$	$s = 0.4$	$s = \infty$	$s = 0.2$	$s = 0.4$	$s = \infty$	$s = 0.2$	$s = 0.4$	$s = \infty$
unit dirs.	0.666 ±0.030	0.497 ±0.028	0.650 ±0.049	0.441 ±0.065	0.507 ±0.105	0.651 ±0.087	0.580 ±0.022	0.619 ±0.008	0.504 ±0.056	0.686 ±0.072	0.631 ±0.018	0.868 ±0.052
	0.287 ±0.010	0.263 ±0.028	0.357 ±0.024	0.312 ±0.048	0.358 ±0.075	0.484 ±0.064	0.341 ±0.018	0.400 ±0.030	0.396 ±0.061	0.266 ±0.029	0.158 ±0.013	0.215 ±0.037
PCA	0.394 ±0.099	0.574 ±0.040	0.674 ±0.012	0.193 ±0.052	0.294 ±0.070	0.390 ±0.109	0.516 ±0.019	0.540 ±0.023	0.642 ±0.007	0.672 ±0.073	0.630 ±0.018	0.870 ±0.049
	0.638 ±0.067	0.617 ±0.018	0.556 ±0.109	0.478 ±0.046	0.551 ±0.040	0.666 ±0.041	0.548 ±0.035	0.623 ±0.021	0.551 ±0.038	0.705 ±0.062	0.644 ±0.019	0.794 ±0.043
ICA	0.702 ±0.035	0.460 ±0.128	0.578 ±0.117	0.470 ±0.035	0.511 ±0.042	0.581 ±0.066	0.619 ±0.024	0.533 ±0.006	0.612 ±0.024	0.650 ±0.072	0.605 ±0.006	0.701 ±0.045
	0.677 ±0.037	0.438 ±0.127	0.609 ±0.131	0.475 ±0.042	0.561 ±0.040	0.644 ±0.055	0.533 ±0.028	0.620 ±0.021	0.559 ±0.040	0.698 ±0.060	0.642 ±0.017	0.785 ±0.046
Grad (OA)	0.645 ±0.067	0.641 ±0.031	0.690 ±0.062	0.547 ±0.056	0.584 ±0.047	0.385 ±0.169	0.629 ±0.033	0.666 ±0.010	0.598 ±0.057	0.717 ±0.059	0.684 ±0.009	0.857 ±0.037
	0.645 ±0.076	0.530 ±0.106	0.548 ±0.114	0.573 ±0.046	0.615 ±0.045	0.631 ±0.128	0.607 ±0.028	0.624 ±0.021	0.584 ±0.039	0.703 ±0.073	0.659 ±0.008	0.771 ±0.029
IG (OA)	0.711 ±0.040	0.593 ±0.094	0.633 ±0.062	0.506 ±0.057	0.600 ±0.027	0.644 ±0.066	0.628 ±0.033	0.670 ±0.014	0.595 ±0.059	0.716 ±0.059	0.682 ±0.010	0.851 ±0.036
	0.677 ±0.037	0.438 ±0.127	0.609 ±0.131	0.475 ±0.042	0.561 ±0.040	0.644 ±0.055	0.533 ±0.028	0.620 ±0.021	0.559 ±0.040	0.698 ±0.060	0.642 ±0.017	0.785 ±0.046

Table 7: Mean ± std. err. of the DCI score of the experiments in Sec. 4.2 for the first correlated component pair (*floor* vs *background* color) in Shapes3D, as an ablation study with further correlations strengths and attribution methods (see Appendix B.7). We observe only small differences between attribution methods, with plain Grad and SG performing best in the DA setting.

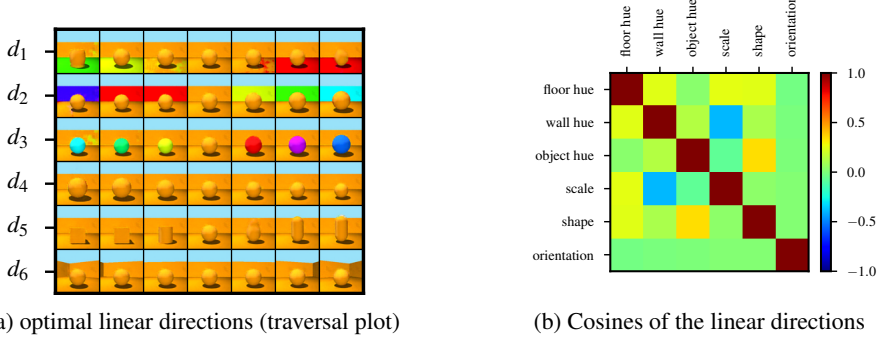


Figure 12: Empirical results for linear entanglement. For the model shown in Fig. 1 (trained on correlated data), we observe almost perfect linear entanglement, i.e., that $f \circ g = D$: (a) There exist linear directions d_1 to d_6 in f 's embedding space that encode the individual components. (b) However, these directions are not necessarily orthogonal; they can be entangled as testified by non-zero cosine distances between them. See Fig. 13 for additional results.

To estimate which factors are changing when a unit direction of the (plain or postprocessed) embedding space is followed (a change in z'_i), we can invert the equation to $z = D^{-1}z'$. The columns in D^{-1} correspond to the change in ground truth components that going one unit in the latent space coordinate i will entail. We refer to this matrix D^{-1} , that shows which ground truth components will be altered by moving along one latent dimension as *linear entanglement matrix*.

Figure 13 shows the traversals along with the corresponding linear entanglement matrices that correspond well to the changes observed. For the plain method, the components that were correlated are deeply entangled (upper line). However, our method (DA, SG, lower line) is able to separate them well, which is testified both by the traversal and the linear disentanglement matrix.

D.6 Further results on CUB

In Tab. 11, we report the quantitative comparison on CUB introduced in Appendix C.6 of our methods with PCA, ICA, and a baseline of randomly sampled directions. ICA failed to discover meaningful components, while PCA

Dataset		Shapes3D			MPI3D-real		
Correlated factors		floor vs. background	orientation vs. background	orientation vs. size	background vs. object color	background vs. robot arm dof-1	robot arm dof-1 vs. robot arm dof-2
BetaVAE	0.309 \pm 0.031	0.426 \pm 0.043	0.335 \pm 0.059	0.232 \pm 0.022	0.185 \pm 0.031	0.196 \pm 0.034	
	+PCA	0.111 \pm 0.031	0.101 \pm 0.009	0.092 \pm 0.031	0.095 \pm 0.010	0.105 \pm 0.023	0.123 \pm 0.033
	+ICA	0.360 \pm 0.040	0.324 \pm 0.054	0.277 \pm 0.036	0.155 \pm 0.025	0.163 \pm 0.014	0.071 \pm 0.014
	+Ours (OA)	0.511 \pm 0.029	0.437 \pm 0.044	0.502 \pm 0.030	0.239 \pm 0.021	0.229 \pm 0.022	0.187 \pm 0.039
	+Ours (DA)	0.594 \pm 0.023	0.485 \pm 0.057	0.545 \pm 0.034	0.193 \pm 0.036	0.092 \pm 0.038	0.080 \pm 0.015
FactorVAE	0.297 \pm 0.084	0.319 \pm 0.076	0.423 \pm 0.018	0.079 \pm 0.001	0.103 \pm 0.020	0.080 \pm 0.010	
	+PCA	0.202 \pm 0.057	0.135 \pm 0.028	0.235 \pm 0.036	0.111 \pm 0.006	0.122 \pm 0.011	0.107 \pm 0.009
	+ICA	0.199 \pm 0.061	0.106 \pm 0.025	0.078 \pm 0.021	0.018 \pm 0.008	0.061 \pm 0.015	0.069 \pm 0.015
	+Ours (OA)	0.337 \pm 0.033	0.322 \pm 0.056	0.288 \pm 0.092	0.070 \pm 0.014	0.086 \pm 0.018	0.039 \pm 0.014
	+Ours (DA)	0.276 \pm 0.036	0.217 \pm 0.064	0.213 \pm 0.036	0.046 \pm 0.021	0.045 \pm 0.016	0.048 \pm 0.015
BetaTCVAE	0.333 \pm 0.008	0.400 \pm 0.046	0.402 \pm 0.017	0.279 \pm 0.025	0.223 \pm 0.030	0.201 \pm 0.039	
	+PCA	0.249 \pm 0.033	0.145 \pm 0.039	0.184 \pm 0.062	0.265 \pm 0.019	0.203 \pm 0.028	0.213 \pm 0.035
	+ICA	0.390 \pm 0.031	0.276 \pm 0.043	0.346 \pm 0.072	0.199 \pm 0.040	0.158 \pm 0.038	0.170 \pm 0.033
	+Ours (OA)	0.484 \pm 0.025	0.490 \pm 0.033	0.526 \pm 0.036	0.092 \pm 0.029	0.071 \pm 0.029	0.041 \pm 0.014
	+Ours (DA)	0.525 \pm 0.014	0.540 \pm 0.021	0.620 \pm 0.024	0.120 \pm 0.037	0.122 \pm 0.044	0.075 \pm 0.028
DipVAE	0.493 \pm 0.032	0.481 \pm 0.020	0.433 \pm 0.044	0.138 \pm 0.020	0.099 \pm 0.040	0.143 \pm 0.045	
	+PCA	0.063 \pm 0.006	0.086 \pm 0.027	0.108 \pm 0.014	0.054 \pm 0.016	0.042 \pm 0.011	0.064 \pm 0.010
	+ICA	0.495 \pm 0.032	0.438 \pm 0.053	0.224 \pm 0.026	0.138 \pm 0.023	0.096 \pm 0.040	0.139 \pm 0.047
	+Ours (OA)	0.512 \pm 0.042	0.425 \pm 0.036	0.465 \pm 0.049	0.146 \pm 0.019	0.105 \pm 0.033	0.136 \pm 0.049
	+Ours (DA)	0.591 \pm 0.028	0.546 \pm 0.017	0.497 \pm 0.060	0.133 \pm 0.029	0.094 \pm 0.036	0.125 \pm 0.045

Table 8: Mean \pm std. err. of the Mutual-Information Gap (MIG) scores of four post-hoc methods applied to the embedding spaces of four disentanglement models on two datasets with different pairs of correlated variables. The MIG is computed across all components of the dataset.

Dataset		Shapes3D			MPI3D-real		
Correlated factors		floor vs. background	orientation vs. background	orientation vs. size	background vs. object color	background vs. robot arm dof-1	robot arm dof-1 vs. robot arm dof-2
BetaVAE	0.834 \pm 0.022	0.839 \pm 0.053	0.828 \pm 0.011	0.557 \pm 0.032	0.490 \pm 0.044	0.412 \pm 0.022	
	+PCA	0.722 \pm 0.060	0.689 \pm 0.047	0.716 \pm 0.035	0.393 \pm 0.037	0.452 \pm 0.031	0.398 \pm 0.031
	+ICA	0.797 \pm 0.036	0.775 \pm 0.083	0.794 \pm 0.022	0.385 \pm 0.100	0.262 \pm 0.061	0.251 \pm 0.031
	+Ours (OA)	0.767 \pm 0.108	0.808 \pm 0.060	0.832 \pm 0.022	0.565 \pm 0.022	0.504 \pm 0.036	0.443 \pm 0.027
	+Ours (DA)	0.813 \pm 0.087	0.829 \pm 0.068	0.826 \pm 0.029	0.567 \pm 0.024	0.525 \pm 0.042	0.444 \pm 0.027
FactorVAE	0.636 \pm 0.045	0.622 \pm 0.064	0.595 \pm 0.050	0.354 \pm 0.016	0.389 \pm 0.015	0.342 \pm 0.006	
	+PCA	0.627 \pm 0.071	0.680 \pm 0.027	0.652 \pm 0.024	0.330 \pm 0.018	0.388 \pm 0.022	0.353 \pm 0.016
	+ICA	0.619 \pm 0.059	0.446 \pm 0.146	0.200 \pm 0.148	0.277 \pm 0.013	0.242 \pm 0.082	0.304 \pm 0.017
	+Ours (OA)	0.663 \pm 0.022	0.661 \pm 0.028	0.644 \pm 0.051	0.347 \pm 0.007	0.386 \pm 0.020	0.337 \pm 0.013
	+Ours (DA)	0.646 \pm 0.026	0.637 \pm 0.023	0.619 \pm 0.026	0.330 \pm 0.015	0.375 \pm 0.016	0.335 \pm 0.013
BetaTCVAE	0.676 \pm 0.012	0.814 \pm 0.052	0.877 \pm 0.015	0.445 \pm 0.044	0.379 \pm 0.021	0.346 \pm 0.020	
	+PCA	0.761 \pm 0.035	0.738 \pm 0.063	0.794 \pm 0.037	0.505 \pm 0.040	0.425 \pm 0.012	0.389 \pm 0.008
	+ICA	0.834 \pm 0.004	0.761 \pm 0.051	0.806 \pm 0.051	0.149 \pm 0.099	0.168 \pm 0.053	0.057 \pm 0.035
	+Ours (OA)	0.837 \pm 0.004	0.849 \pm 0.015	0.879 \pm 0.013	0.463 \pm 0.048	0.401 \pm 0.018	0.399 \pm 0.019
	+Ours (DA)	0.842 \pm 0.000	0.854 \pm 0.017	0.878 \pm 0.013	0.460 \pm 0.046	0.399 \pm 0.018	0.399 \pm 0.014
DipVAE	0.826 \pm 0.006	0.839 \pm 0.006	0.785 \pm 0.033	0.517 \pm 0.046	0.473 \pm 0.046	0.430 \pm 0.013	
	+PCA	0.671 \pm 0.019	0.603 \pm 0.064	0.653 \pm 0.039	0.431 \pm 0.028	0.373 \pm 0.027	0.344 \pm 0.021
	+ICA	0.826 \pm 0.006	0.831 \pm 0.007	0.749 \pm 0.027	0.434 \pm 0.042	0.423 \pm 0.027	0.424 \pm 0.012
	+Ours (OA)	0.824 \pm 0.007	0.812 \pm 0.018	0.785 \pm 0.029	0.503 \pm 0.044	0.471 \pm 0.035	0.436 \pm 0.021
	+Ours (DA)	0.822 \pm 0.006	0.850 \pm 0.012	0.809 \pm 0.045	0.505 \pm 0.040	0.459 \pm 0.040	0.448 \pm 0.026

Table 9: Mean \pm std. err. of the FactorVAE scores of four post-hoc methods applied to the embedding spaces of four disentanglement models on two datasets with different pairs of correlated variables. The FactorVAE score is computed across all components of the dataset.

Dataset		Shapes3D			MPI3D-real		
Correlated factors		floor vs. background	orientation vs. background	orientation vs. size	background vs. object color	background vs. robot arm dof-1	robot arm dof-1 vs. robot arm dof-2
BetaVAE	0.086 ± 0.003	0.119 ± 0.004	0.100 ± 0.005		0.127 ± 0.014	0.098 ± 0.015	0.092 ± 0.025
	+PCA	0.047 ± 0.005	0.062 ± 0.006	0.066 ± 0.006	0.027 ± 0.005	0.055 ± 0.008	0.037 ± 0.006
	+ICA	0.007 ± 0.001	0.013 ± 0.001	0.019 ± 0.004	0.017 ± 0.006	0.007 ± 0.002	0.004 ± 0.001
	+Ours (OA)	0.099 ± 0.026	0.114 ± 0.008	0.112 ± 0.007	0.131 ± 0.011	0.113 ± 0.005	0.082 ± 0.024
	+Ours (DA)	0.094 ± 0.020	0.127 ± 0.012	0.114 ± 0.013	0.107 ± 0.025	0.059 ± 0.024	0.037 ± 0.013
FactorVAE	0.072 ± 0.006	0.059 ± 0.006	0.064 ± 0.001		0.059 ± 0.004	0.066 ± 0.008	0.054 ± 0.003
	+PCA	0.060 ± 0.006	0.066 ± 0.004	0.057 ± 0.004	0.065 ± 0.008	0.076 ± 0.004	0.071 ± 0.003
	+ICA	0.013 ± 0.002	0.008 ± 0.001	0.006 ± 0.002	0.002 ± 0.000	0.002 ± 0.001	0.001 ± 0.000
	+Ours (OA)	0.077 ± 0.012	0.052 ± 0.005	0.054 ± 0.017	0.054 ± 0.006	0.059 ± 0.006	0.036 ± 0.015
	+Ours (DA)	0.071 ± 0.014	0.053 ± 0.012	0.040 ± 0.010	0.041 ± 0.017	0.043 ± 0.015	0.044 ± 0.013
BetaTCVAE	0.052 ± 0.002	0.107 ± 0.013	0.096 ± 0.016		0.151 ± 0.017	0.133 ± 0.007	0.117 ± 0.011
	+PCA	0.073 ± 0.004	0.075 ± 0.011	0.107 ± 0.015	0.148 ± 0.018	0.125 ± 0.009	0.109 ± 0.007
	+ICA	0.015 ± 0.000	0.010 ± 0.001	0.011 ± 0.002	0.011 ± 0.004	0.005 ± 0.002	0.004 ± 0.002
	+Ours (OA)	0.105 ± 0.003	0.119 ± 0.012	0.130 ± 0.023	0.055 ± 0.017	0.059 ± 0.016	0.056 ± 0.003
	+Ours (DA)	0.108 ± 0.005	0.127 ± 0.013	0.109 ± 0.017	0.071 ± 0.020	0.072 ± 0.010	0.051 ± 0.015
DipVAE	0.083 ± 0.004	0.084 ± 0.003	0.070 ± 0.002		0.056 ± 0.011	0.039 ± 0.013	0.057 ± 0.016
	+PCA	0.027 ± 0.003	0.034 ± 0.006	0.043 ± 0.004	0.023 ± 0.004	0.030 ± 0.008	0.022 ± 0.005
	+ICA	0.006 ± 0.001	0.003 ± 0.002	0.030 ± 0.002	0.011 ± 0.005	0.005 ± 0.003	0.005 ± 0.002
	+Ours (OA)	0.089 ± 0.012	0.082 ± 0.005	0.077 ± 0.002	0.060 ± 0.008	0.047 ± 0.010	0.061 ± 0.016
	+Ours (DA)	0.114 ± 0.003	0.105 ± 0.008	0.084 ± 0.007	0.051 ± 0.008	0.043 ± 0.012	0.054 ± 0.016

Table 10: Mean ± std. err. of the SAP scores of four post-hoc methods applied to the embedding spaces of four disentanglement models on two datasets with different pairs of correlated variables. The SAP score is computed across all components of the dataset.

was only capable of discovering very few high-variance ones in the beginning, but begins to fail for $K > 10$. This is possibly because in PCA, the directions are required to be orthogonal. Surprisingly, both PCA and ICA were not much better than the random baseline. Our method constantly discovered components and surpassed all three baselines. In particular, our method (DA) with Integrated Gradient attributions instead of plain gradients (see Appendix B.7) leads to good performance. This leads us to the hypotheses that for high-dimensional data, (1) the disjointness principle is required to identify solutions and (2) that the gradients need to be smoothed or aggregated by some technique such as IG or SG. Figure 14 illustrates the correlation between the ground-truth attribute representation (scores) and predicted representation by using our model (using plain gradients) for the top discovered component. The two components are clearly correlated, but more in a block-sense: Classes with low scores on the attribute received low scores on the discovered component. The same holds for high scores, but within these, we observe stronger noise, which explains why the Spearman’s correlation values were imperfect. This can be due to a certain degree of arbitrage in the ground-truth attribute values of each class. Here, Fig. 15, just like Fig. 5 in the main paper, shows qualitative examples, including the ground-truth values which appear to fluctuate. We emphasize that this analysis should be viewed as a take on quantifying the quality of interpretable components, but that a refined benchmark is material for future work.

Num. components	K=1	K=10	K=20	K=30	K=40	K=50	K=60
Baseline (random)	0.659 ± 0.017	0.618 ± 0.012	0.585 ± 0.011	0.559 ± 0.011	0.536 ± 0.010	0.516 ± 0.009	0.492 ± 0.010
PCA	0.789 ± 0.024	0.602 ± 0.007	0.497 ± 0.005	0.440 ± 0.006	0.402 ± 0.004	0.372 ± 0.004	0.346 ± 0.004
ICA	0.515 ± 0.028	0.442 ± 0.005	0.412 ± 0.006	0.390 ± 0.007	0.370 ± 0.007	0.353 ± 0.007	0.335 ± 0.006
Ours-OA,Grad	0.657 ± 0.025	0.601 ± 0.009	0.564 ± 0.009	0.535 ± 0.008	0.510 ± 0.009	0.488 ± 0.010	0.463 ± 0.012
Ours-OA,IG	0.705 ± 0.044	0.613 ± 0.015	0.569 ± 0.012	0.541 ± 0.011	0.517 ± 0.010	0.493 ± 0.008	0.468 ± 0.006
Ours-OA,SG	0.653 ± 0.026	0.599 ± 0.010	0.563 ± 0.007	0.553 ± 0.015	0.534 ± 0.014	0.515 ± 0.015	0.469 ± 0.007
Ours-DA,Grad	0.701 ± 0.045	0.626 ± 0.029	0.585 ± 0.028	0.559 ± 0.011	0.535 ± 0.029	0.515 ± 0.030	0.490 ± 0.030
Ours-DA,IG	0.710 ± 0.020	0.657 ± 0.008	0.615 ± 0.013	0.587 ± 0.016	0.562 ± 0.018	0.539 ± 0.021	0.514 ± 0.021
Ours-DA,SG	0.686 ± 0.020	0.641 ± 0.031	0.610 ± 0.032	0.584 ± 0.032	0.561 ± 0.033	0.540 ± 0.033	0.516 ± 0.033

Table 11: Quantitative comparison of discovered components using our methods, PCA, ICA and a random baseline. Mean correlation score of top-K (K in column) discovered components are shown in (mean ± std.) for five runs.

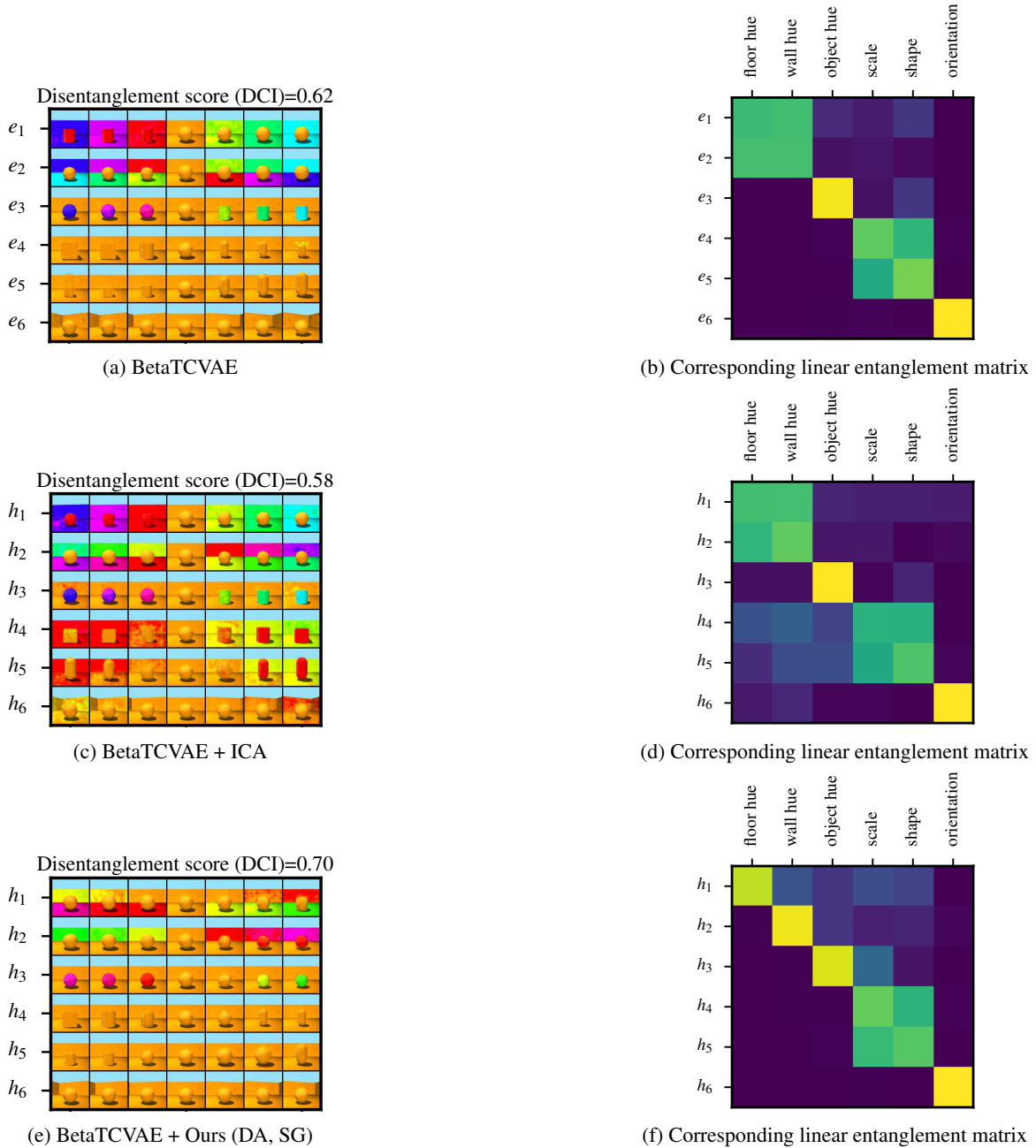


Figure 13: Traversal plots from another model (BetaTCVAE) trained on the correlated dataset. As for all traversal plots in this paper, we manually permuted the dimensions to match across plots. In addition, we compute a matrix of linear entanglement that shows which ground truth factors is changed when moving into a certain direction (brightness corresponds to magnitude of change). While none of the post-hoc methods manages to disentangle shape and size (most likely due to their non-linear encoding), our model resolves the linearly entangled factors *floor hue* and *wall hue* fairly well, which can also be seen from the entanglement matrix.

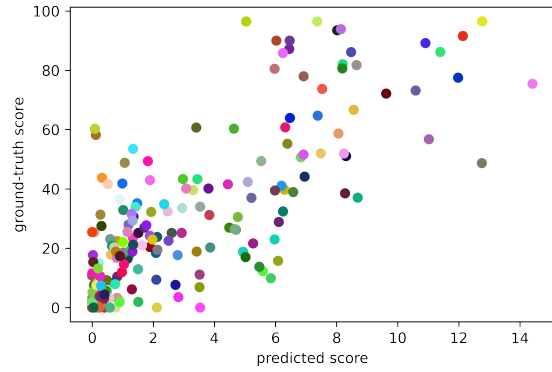


Figure 14: Correlation between ground-truth attribute scores and our predicted scores for the best matched component. Each dot represents a class.

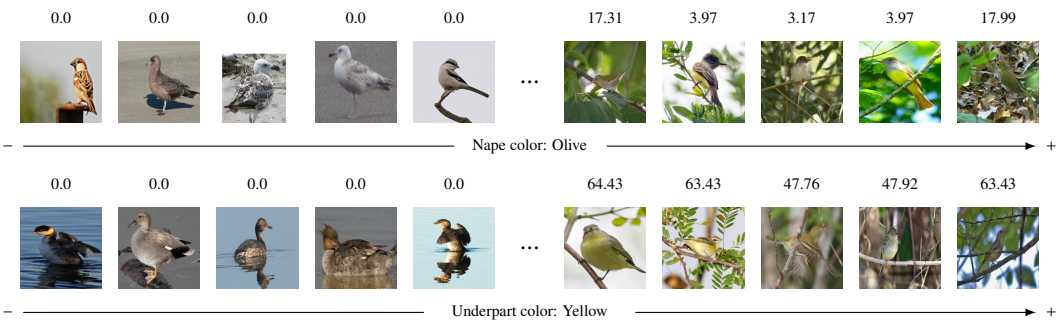


Figure 15: Examples of discovered components on CUB. The corresponding ground-truth attribute is shown under images and the ground-truth value of each image is depicted above the image. “+/-” indicate the positive/negative direction along the discovered concept.